



CANCER

Intertumoral lineage diversity and immunosuppressive transcriptional programs in well-differentiated gastroenteropancreatic neuroendocrine tumors

Samantha E. Hoffman^{1,2,3,4}, Todd W. Dowrey^{5,6}, Carlos Villacorta Martin⁶, Kevin Bi^{1,2}, Breanna Titchen^{1,2,4}, Shreya Johri^{1,2,4}, Laura DelloStritto⁷, Miraj Patel^{1,8,9}, Colin Mackichan^{1,8†}, Stephanie Inga^{1,8,9}, Judy Chen^{1,8,9‡}, Grace Grimaldi^{1,8§}, Sara Napolitano^{1,2,8}, Isaac Wakiro^{1,2§}, Jingyi Wu^{1,2,8¶}, Jason Yeung^{1,2,8#}, Asaf Rotem^{1,2,8**}, Ewa Sicinska⁹, Erin Shannon^{1,2}, Thomas Clancy¹⁰, Jiping Wang¹⁰, Sarah Denning¹, Lauren Brais¹, Naomi R. Besson¹¹, Kathleen L. Pfaff¹¹, Ying Huang¹²⁺⁺, Katrina Z. Kao^{9,11}, Scott Rodig⁹, Jason L. Hornick⁹, Sebastien Vigneau^{1,2,8‡‡}, Jihye Park^{1,2}, Matthew H. Kulke⁵, Jennifer Chan^{1§§}, Eliezer M. Van Allen^{1,2*§§}, George J. Murphy^{5,6*§§}

Neuroendocrine tumors (NETs) are rare cancers that most often arise in the gastrointestinal tract and pancreas. The fundamental mechanisms driving gastroenteropancreatic (GEP)–NET growth remain incompletely elucidated; however, the heterogeneous clinical behavior of GEP–NETs suggests that both cellular lineage dynamics and tumor microenvironment influence tumor pathophysiology. Here, we investigated the single-cell transcriptomes of tumor and immune cells from patients with gastroenteropancreatic NETs. Malignant GEP–NET cells expressed genes and regulons associated with normal, gastrointestinal endocrine cell differentiation, and fate determination stages. Tumor and lymphoid compartments sparsely expressed immunosuppressive targets commonly investigated in clinical trials, such as the programmed cell death protein–1/programmed death ligand–1 axis. However, infiltrating myeloid cell types within both primary and metastatic GEP–NETs were enriched for genes encoding other immune checkpoints, including *VSIR* (VISTA), *HAVCR2* (TIM3), *LGALS9* (Gal-9), and *SIGLEC10*. Our findings highlight the transcriptomic heterogeneity that distinguishes the cellular landscapes of GEP–NET anatomic subtypes and reveal potential avenues for future precision medicine therapeutics.

INTRODUCTION

Neuroendocrine tumors (NETs) are rare cancers of the diffuse neuroendocrine system, and while they represent less than 1% of all newly diagnosed malignancies in the United States per year, the population prevalence is estimated to exceed 100,000 individuals (1–3). The diagnosed incidence of GEP–NETs has risen markedly over the past four decades, a persistent trend ascribed partially to improved tumor classification and diagnostic technologies (1, 2, 4). Approximately two-thirds of all NETs are gastroenteropancreatic (GEP) in origin, predominantly in the pancreas (12 to 30% of GEP–NETs), stomach, and small intestine (31 to 50% of GEP–

NETs) of older adults (3, 5). While patients with localized disease can be cured with surgical resection, these tumors are often identified at a late clinical stage. Despite rapid advancements in NET research and clinical investigation, treatment options for such patients remains limited (5).

A limiting factor in developing novel therapies for NETs is that the fundamental biology of GEP–NETs remains incompletely understood. Previous investigations have been challenged by limited tissue availability and a scarcity of representative in vitro and in vivo experimental models. Characteristic genomic mutations in these tumors most often occur in tumor suppressor genes

¹Department of Medical Oncology, Dana-Farber Cancer Institute, Harvard Medical School, Boston, MA 02115, USA. ²Broad Institute of Harvard and MIT, Cambridge, MA 02142, USA. ³Harvard-MIT MD-PhD Program, Harvard Medical School, Boston, MA 02115, USA. ⁴PhD Program in Biological and Biomedical Sciences, Division of Medical Sciences, Harvard Medical School, Boston, MA 02115, USA. ⁵Section of Hematology and Medical Oncology, Boston University School of Medicine and Boston Medical Center, Boston, MA 02118, USA. ⁶Center for Regenerative Medicine, Boston University and Boston Medical Center, Boston, MA 02118, USA. ⁷Harvard Pilgrim Health Care Institute, Boston, MA 02215, USA. ⁸Center for Cancer Genomics, Dana-Farber Cancer Institute, Boston, MA 02115, USA. ⁹Department of Pathology, Brigham and Women's Hospital, Harvard Medical School, Boston, MA 02115, USA. ¹⁰Department of Surgery, Brigham and Women's Hospital, Harvard Medical School, Boston, MA 02115, USA. ¹¹Center for Immuno-Oncology, Dana-Farber Cancer Institute, Boston, MA 02115, USA. ¹²Molecular Pathology Core Laboratory, Dana-Farber Cancer Institute, Boston, MA 02115, USA.

*Corresponding author. Email: eliezerm_vanallen@dfci.harvard.edu (E.M.V.A.); gjmurphy@bu.edu (G.J.M.)

†Present address: Viome, Bothell, WA 98011, USA.

‡Present address: Yale School of Public Health, New Haven, CT 06510, USA.

§Present address: Memorial Sloan Kettering Cancer Center, New York, NY 10065, USA.

¶Present address: University of Rochester, Rochester, NY 14627, USA.

#Present address: Boston University, Boston, MA 02215, USA.

**Present address: AstraZeneca, Waltham, MA 02451, USA.

++Present address: Novartis Institutes for BioMedical Research, Cambridge, MA 02139, USA.

‡‡Present address: Ginkgo Bioworks, Boston, MA 02210, USA.

§§These authors contributed equally to this work.

Copyright © 2023 The Authors, some rights reserved; exclusive licensee American Association for the Advancement of Science. No claim to original U.S. Government Works. Distributed under a Creative Commons Attribution NonCommercial License 4.0 (CC BY-NC).

associated with hereditary endocrine cancer syndromes, including multiple endocrine neoplasia type 1 (*MEN1*), von Hippel-Lindau disease (*VHL*), or tuberous sclerosis (*TSC1/2*) (6). Chromosomal loss, telomere alterations, and epigenetic modifications have emerged as potential regulators of GEP-NET development but are not sufficiently targeted by currently available treatments (7, 8). The inter- and intratumoral heterogeneity of GEP-NETs at different anatomical sites (e.g., pancreas, small intestine, and stomach) poses an additional challenge to understanding the oncogenic mechanisms driving tumor formation in these disparate environments.

High-resolution delineation of the tumor and immune niches of GEP-NETs has the potential to elucidate previously unknown, actionable targets for future precision medicine endeavors, expanding the limited menu of therapeutic options available to patients with nonresectable tumors. Previous investigations to this end have used immunohistochemical or bulk RNA sequencing approaches, but these methodologies are insufficient to identify rare or unknown cell states that contribute to tumor biology and progression. Single-cell RNA sequencing (scRNA-seq) of other gastrointestinal solid tumors has enabled high-resolution characterization of the cell subpopulations within the cancer microenvironment, thereby overcoming the challenges presented by older technologies (9–12). We therefore hypothesized that dissecting the transcriptomic landscape of GEP-NETs at single-cell resolution would elucidate shared and distinct cellular phenotypes and genetic programming among these heterogeneous tumors.

RESULTS

Characterizing the cellular landscape of GEP-NETs

We collected fresh surgical resection specimens from eight patients with well-differentiated NETs, comprising four pancreatic NETs (pNETs), three small intestinal NETs (siNETs), and one gastric NET (gNET). The siNET and gNET samples included tissue from regional extension of the primary tumor. Resection tissue was dissociated and divided in two for parallel processing; one-half of each cell suspension sorted for viability using flow cytometry for scRNA-seq using the 10x Genomics platform, while the other was flow sorted for both CD45 positivity and viability before undergoing 10x processing (Fig. 1A and Methods). Of the eight samples in our cohort, five had received no previous therapy, while the remaining three tumors had been treated with the somatostatin analog lanreotide. The gNET had been treated with both lanreotide and everolimus and chemotherapy with capecitabine and temozolomide (Fig. 1B). Our cohort also included one primary-metastasis pair from the same patient (sinet2 and sinet3; Fig. 1B).

After preprocessing and quality control, our single-cell atlas contained high-quality transcriptomes from 24,048 cells spanning both tumor and immune compartments (Fig. 1C and Methods). Across-dataset integration of all cells (CD45⁺ sorted and non-CD45⁺ sorted) was performed using the Harmony algorithm to mitigate batch effects stemming from technical or biological variances between individual patients, tissue collection, and sample processing (Fig. 1, C and D, and Methods). Using differential gene expression analysis, we identified cluster-specific marker genes that enabled us to subcategorize the lymphoid and myeloid immune compartments (Fig. 1C and fig. S1A). Tumor cells were identified as cells differentially expressing NET-related marker genes and

demonstrating inferred copy number variation compared to reference normal cells (fig. S1C and Methods).

We then compared the microenvironmental composition of GEP-NETs from distinct sites of origin (Fig. 1E). In general, myeloid cells including macrophages, monocytes, and dendritic cells (DCs) represented the largest immune subpopulation within pNETs, while siNETs and the gNET contained a relatively higher proportion of T cells and natural killer (NK) cells (Fig. 1E). Cell type proportions varied between GEP-NETs from the same site of origin, reflecting the intrinsic heterogeneity of these tumors.

Differential expression analysis and gene regulatory network inference reveal multilineage profiles of pNETs

We next interrogated the transcriptional landscapes of GEP-NET cells from different anatomical sites of origin (Fig. 2A). All tumors expressed known NET markers such as chromogranin genes *CHGA* and *CHGB* (Fig. 2B). While most tumors expressed somatostatin receptor 2 (*SSTR2*), no GEP-NET expressed *SSTR5* (Fig. 2B). We also interrogated commonly mutated genes in pNETs to assess their expression levels across GEP-NETs. *ATRX*, a somatic mutation identified in pNETs, was heterogeneously expressed across GEP-NET subtypes; *DAXX*, conversely, was either minimally or not expressed by any tumor (Fig. 2B). Mutations of *ATRX* and *DAXX* in pNETs are often inactivating or missense in nature, which could explain the paucity of expression we identified here (13).

To compare the transcriptional profiles of pNETs and siNETs, we then performed differential gene expression on all tumor cells from those anatomical sites. Primary and metastatic siNETs exhibited relatively homogeneous transcriptional landscapes compared to pNETs and featured genes involved in monoamine and hormone synthesis (e.g., *TAC1* and *TPH1*) and neuroendocrine transport and vesicle release (e.g., *SYT13* and *SLC18A1*) (Fig. 2C), concordant with established profiles of carcinoid tumors. The pNETs in our cohort displayed marked intertumoral heterogeneity, with few differentially expressed genes common to all four tumors (Fig. 2C). However, all pNETs expressed genes involved in pancreas exocrine (e.g., *CCK* and *SPINK1*) and endocrine function (e.g., *INS*, *VIP*, *GCG*, and *PPY*) (Fig. 2C). The neuroendocrine genes expressed by each tumor corresponded closely to its clinical profile; for example, pnet2 demonstrated the highest expression of the insulin-encoding gene *INS*, matching its pathological characterization as a well-differentiated insulinoma (Fig. 2C).

Next, we sought to identify regulatory elements underlying the heterogeneous molecular profiles of GEP-NETs from different anatomical sites. To this end, we performed single-cell regulatory network inference and clustering (SCENIC) analysis on malignant cells from each tumor. We identified the top regulons for each tumor by the area under the curve (AUC) value as calculated by the standard pySCENIC workflow (Fig. 2D and Methods). Hierarchical clustering of NETs by regulon activity produced two major subgroups that did not segregate solely by anatomical location; the first contained most pNETs and the gNET sample, while the other comprised all siNETs and pnet1. Within our pNET samples, one tumor (pnet2) displayed differential activity of the transcription factors (TFs) *PDX1*, *PAX6*, *MAFA*, *NKX6-1*, and *RXRG* (Fig. 2D). These TFs are known regulators of beta cell fate in healthy human pancreatic islets, consistent with the clinical diagnosis of insulinoma (14–17). Another pNET (pnet1) displayed differential activity of

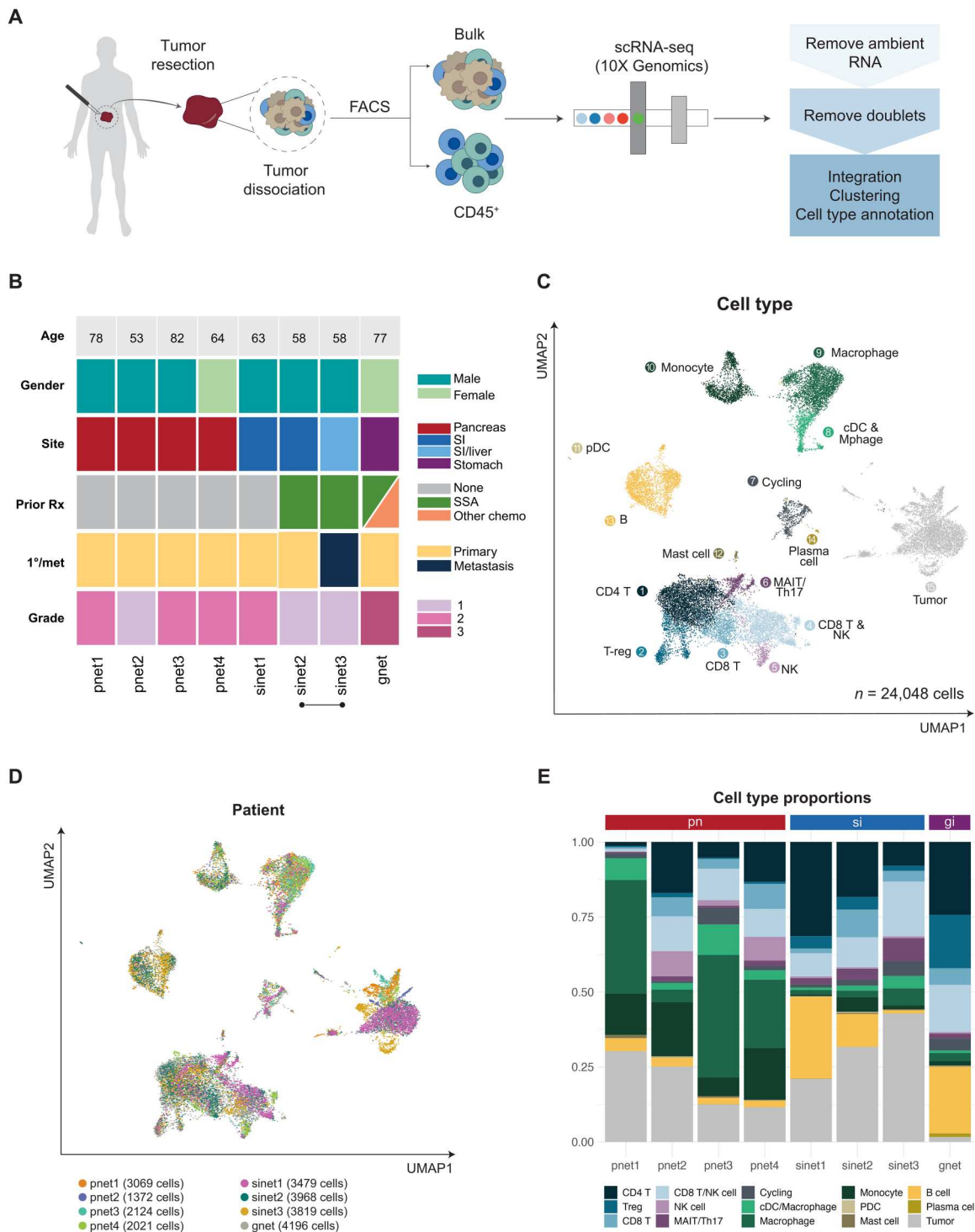


Fig. 1. Characterizing the cellular landscape of pancreatic, small intestinal, and gNETs. (A) NET scRNA-seq workflow. Resected tumor fragments were dissociated into single-cell suspensions, which were then divided for parallel sequencing of (i) nonsorted single cells and (ii) fluorescence-activated cell sorting (FACS) sorted, CD45⁺ immune cells. All samples were processed using the 10x Genomics platform. (B) Patient demographics and treatment summary at time of tumor resection. Site: SI, small intestine; SI/liver: small intestinal primary tumor with liver metastasis. A bar underneath samples indicates that they originate from the same patient. (C) UMAP of malignant and nonmalignant cells from all tumors, colored by general cell type. (D) UMAP of malignant and nonmalignant cells from all tumors, colored by sample of origin (left). (E) Cellular composition of each tumor, colored by general cell type.

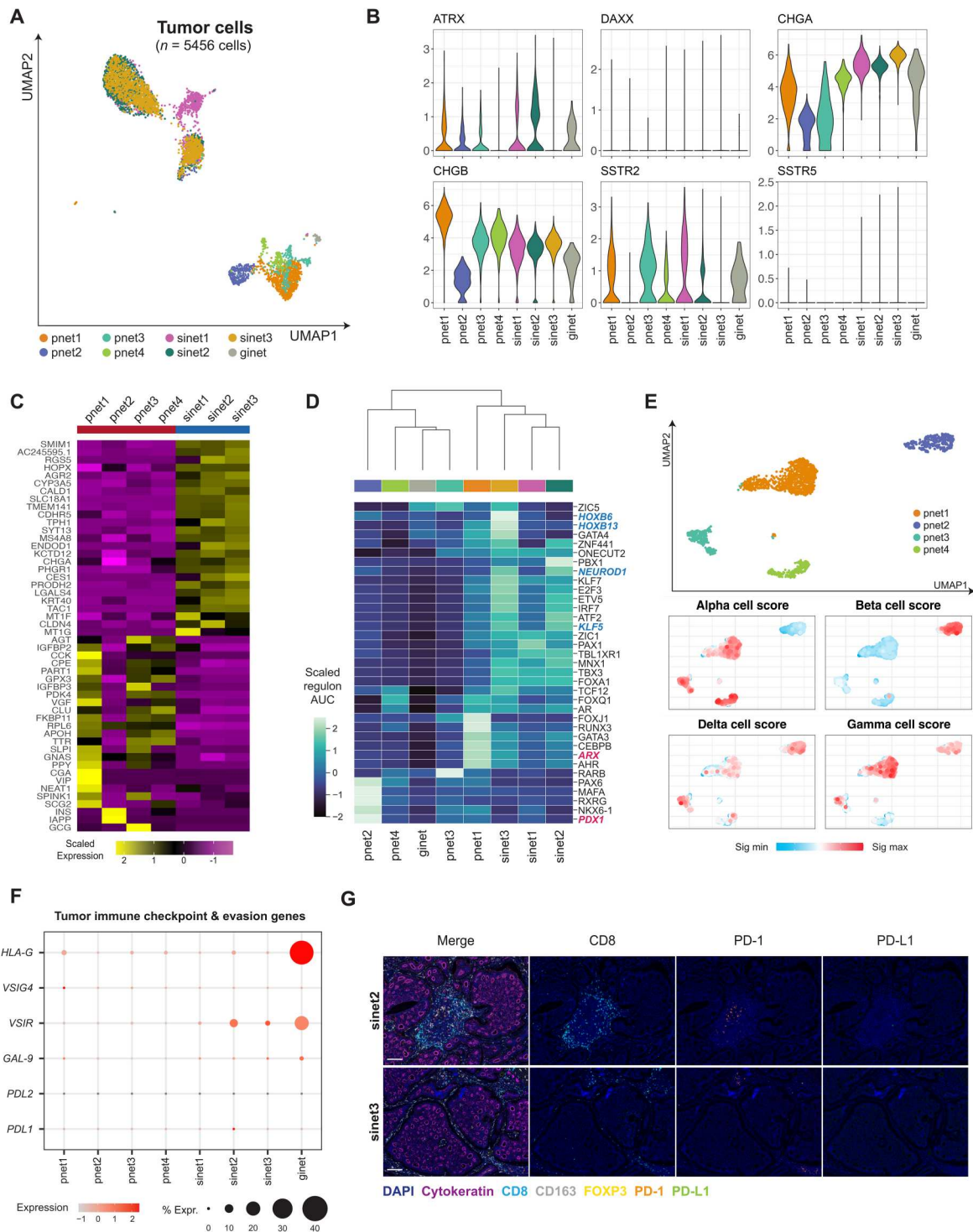


Fig. 2. GEP-NET cells do not express common immune checkpoint targets. (A) UMAP plot of all malignant cells from all GEP-NET samples, colored by sample of origin. (B) Violin plots of genes commonly expressed in GEP-NETs, grouped and colored by sample. (C) Heatmap of scaled, normalized average expression of top 50 differentially expressed genes between pancreatic (pn) and small intestinal (si) NETs. (D) Heatmap of scaled expression of the top five differentially expressed regulons per individual tumor. Blue-labeled genes indicate involvement in enteroendocrine differentiation or regulation of intestinal stem cell fate. Red-labeled genes indicate TFs with known involvement in endocrine pancreas development and pNET biology. (E) UMAP plots of malignant cells from all pNETs, colored by tumor of origin (top), followed by heatmaps in UMAP space of VISION signature scores for cell type-specific genes for the major cells in the normal human endocrine pancreas (bottom). (F) Dotplot of percent expression of common, targetable immune checkpoint and evasion genes, grouped by sample. (G) Representative immunohistochemical staining of CD8, PD-1, and PD-L1 two siNET samples. PD-1 and PD-L1 expression was low to nonexistent across all stained samples, consistent with low transcriptional expression by scRNA-seq. Scale bars, 100 μ m. DAPI, 4',6'-diamidino-2-phenylindole.

the *ARX* TF, which primarily directs pancreas alpha cell development but also has known roles in establishing pancreatic gamma cell fate in healthy islets of Langerhans (Fig. 2D) (18, 19). These data are consistent with a previous investigation of enhancer profiles of nonfunctional pNETs, which found that those tumors could be stratified into two major groups by *PDX1* and *ARX* activity (19). However, two of our pNETs did not express either *PDX1* or *ARX*. Pnet4 displayed differential activity of *TCF12*, which has been implicated in pancreatic and gastrointestinal cancer proliferation and invasion, while pnet3's top regulon, *RARB*, was previously found to direct differentiation of embryonic stem cells to pancreatic endocrine cells in vitro (20, 21). Few common TFs were identified across NET samples, revealing the heterogeneity within and between GEP-NETs from different anatomical sites.

Within our siNET samples, we identified differential activity of TFs associated with regulation of enteroendocrine cell lineages (*NEUROD1* and *FOXA1*) and with the maintenance of intestinal stem cell fate (*KLF5*), concordant with a leading hypothesis in the field of NET biology that siNETs develop from enterochromaffin cells in the gut (Fig. 2D) (22–24). The lone siNET metastasis sample (sinet3) displayed highly differential activity of homeobox (*HOX*) TFs, including *HOXB6* and *HOXB13* (Fig. 2D). Previous analysis of primary human fetal small intestinal tissue revealed that *HOXB* gene expression is strongest early in duodenal development but quickly diminishes over time (25). The *HOXB* family was not represented amongst the top regulons for either primary siNET in our cohort, suggesting that the siNET metastasis may have undergone dedifferentiation to resemble an earlier stage of small intestinal fate determination (Fig. 2D).

To determine the transcriptional similarity of our four pNET tumors to healthy, mature pancreatic islet cells, we scored malignant cells from each tumor with curated gene signatures specific to alpha, beta, gamma, and delta cells in mature human pancreatic islets (Fig. 2E) (26). Tumor cells from pnet1 displayed robust expression of alpha cell and gamma cell gene signatures, with lower expression of the delta cell signature (Fig. 2E); these findings are consistent with the robust expression of gamma and delta cell hormones *PPY* and *VIP* and elevated *ARX* TF activity identified in our previous analyses. Similarly, as predicted by the results of our differential gene expression and gene regulatory network (GRN) analysis, pnet2 was the tumor with the highest expression score for the beta cell signature (Fig. 2E). Pnet3 and pnet4 scored most highly for the alpha cell signature with lower expression of delta and gamma cell scores (Fig. 2E). Together with the results of our regulatory network analysis, these data demonstrate tumor cell resemblance to earlier stages of gastrointestinal development and the potential for lineage plasticity in these rare tumors.

GEP-NET cells do not express classical immune checkpoint blockade targets

The success and ongoing studies of immunotherapy in other solid tumor types have motivated a strong interest in applying this therapeutic approach to the treatment of GEP-NETs. We therefore next sought to quantify the expression of classical, tumor cell–anchored immunotherapy targets across the GEP-NETs (Fig. 2F). Programmed death ligand–2 (*PDL2*), which binds programmed cell death protein 1 (PD-1) on the surface of T cells to suppress antitumor immunity, was not expressed in any GEP-NETs in our cohort. *PDL1*, which also binds to PD-1 to negatively regulate T

cell immunity, was expressed at low levels in fewer than half of tumors. Although roughly 40% of gNET cells expressed *HLA-G*, a recently described immunomodulatory ligand, all other tumors rarely expressed this gene; anatomical location, pathological grade, and treatment history may therefore drive this differential expression (27). *LGALS9* (also known as Gal-9), *VSIG*, and *VSIR*, other regulators of T cell anergy and exhaustion, were also sparsely expressed but were identified in a greater proportion of tumors than *PDL1*.

Next, we sought to validate the low expression of the PD-1/PD-L1 immunosuppressive axis in GEP-NETs at the protein level. To do this, we performed multiplex immunofluorescence staining of PD-1 and PD-L1 in formalin-fixed, paraffin-embedded (FFPE) tissue from small intestinal and pNETs in our cohort using the ImmunoProfile platform (28). Across all stained samples, we identified very few PD-1– or PD-L1–positive cells in the tumor microenvironment and found no positive cells in the tumor compartment (Fig. 2G and fig. S2, A to C). Together, our observations can inform future clinical investigation into the use of anti-PD-1/PD-L1 immunotherapies versus emerging immunotherapy options in patients with well-differentiated GEP-NETs.

Given the demonstrated efficacy of the mammalian target of rapamycin (mTOR) inhibitor everolimus in the treatment of patients with advanced GEP-NETs, we also investigated the expression of mTOR pathway genes in our cohort (29). We scored all malignant cells with the “PI3K/AKT/mTOR Signaling” gene signature from the HALLMARK collection in Molecular Signatures Database (MSigDb; fig. S2, D and E) and performed pairwise score comparisons to establish the significance of expression differences (Wilcoxon two-sided test, $P < 0.05$). The siNETs and gNET in our cohort scored significantly higher for the PI3K/AKT/mTOR Signaling signature compared to the pNETs (fig. S2D). The metastatic tumor sinet3 had a lower signature score than its primary counterpart (sinet2). Functional follow-up will be required to determine the correlation between gene signature score and everolimus response across GEP-NET subtypes, but our findings demonstrate heterogeneity in mTOR signaling across GEP-NETs from different sites of origin.

Profiling lymphoid cell heterogeneity in GEP-NETs

To better understand the immune microenvironment of GEP-NETs, we next analyzed the lymphoid compartment of our dataset. We selected all T and NK cells from the full scRNA-seq atlas using canonical marker genes (fig. S1A and Methods) for de novo clustering and differential gene expression analysis (fig. S3, A and B). We identified diverse T and NK cell populations including NK cells (*FGFBP2*⁺ and *FGFBP2*[−]), resting and effector CD4⁺ T cells, regulatory T cells (T_{regs}), CD8⁺ T cells, T helper 17 cells (T_H17), and mucosal-associated invariant T cells (MAITs) (Fig. 3, A and B). These T and NK cell types were identified in differing proportions across GEP-NET site of origin, with the gNET containing the highest proportion of T_{regs} across samples (Fig. 3A). We also classified B cells from our original dataset, the majority of which originated in either the gNET or siNETs (fig. S3C). Of the six B cell clusters identified in our analysis, two contained *IL4R*-expressing naïve B cells, while the other four comprised *CD27*-expressing memory B cells (fig. S3, D and E).

The higher expression of immune checkpoint genes in 4-1BB-hi CD8⁺ T cells compared to other CD8⁺ T cells across all GEP-NETs

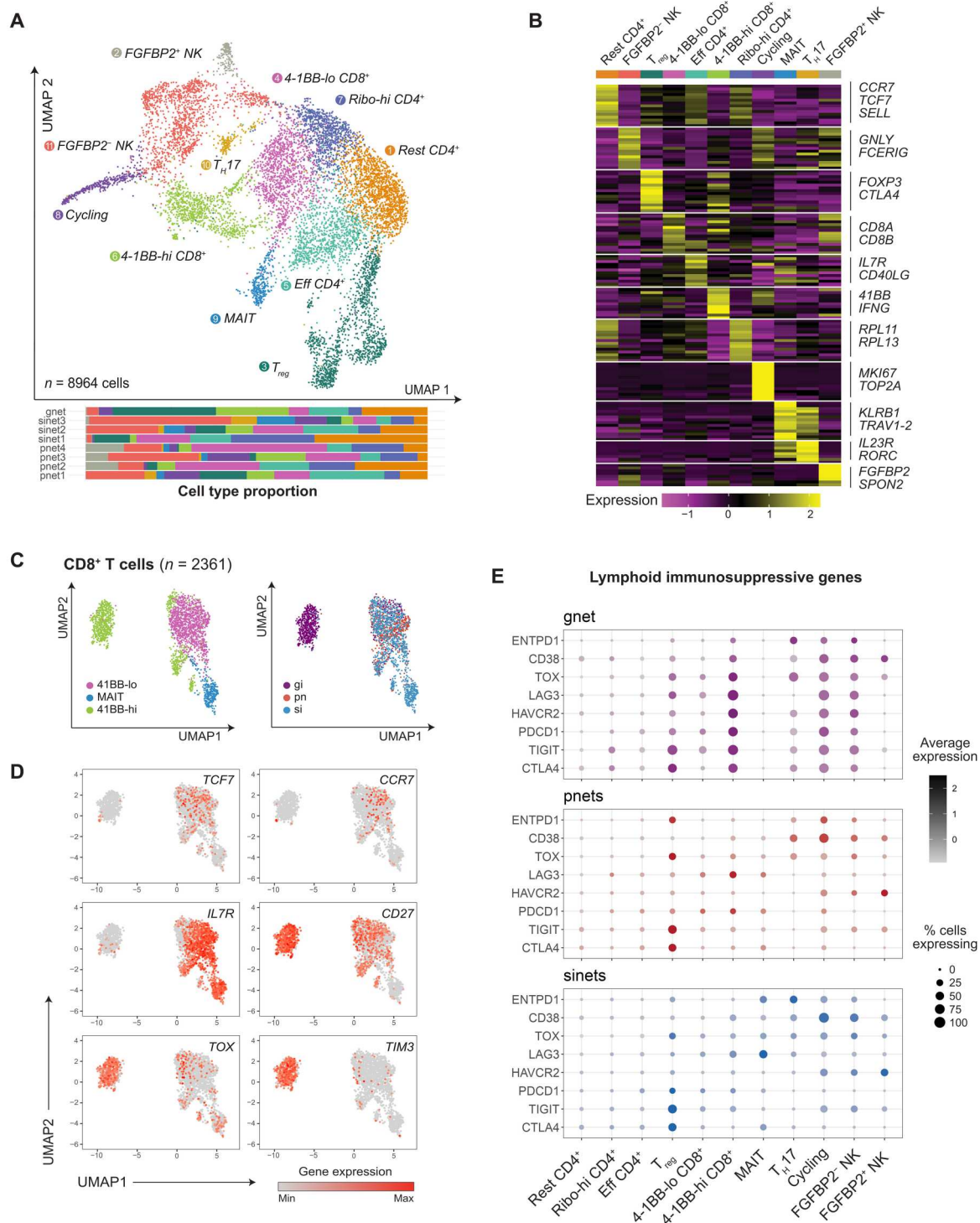


Fig. 3. Classifying T cell and NK cell populations within GEP-NETs. (A) UMAP (top) of T cells and NK cells from all tumors, colored and labeled by lymphoid subtype. Barplot (bottom) displays T/NK cell type proportion by sample. (B) Heatmap of scaled, normalized expression of top 15 differentially expressed genes per T/NK cell subtype. Specific subtype-determining genes are annotated at right. (C) UMAP of CD8⁺ T cells from all tumors, colored by CD8⁺ T cell subtype (left) and NET origin site (right). (D) Expression heatmaps in UMAP space of naïve (*TCF7* and *CCR7*), memory (*IL7R*), and exhausted (*TOX*) CD8 T cell markers as well as coinhibitory receptor *TIM3* in CD8⁺ T cells. (E) Dotplots of percent of T cell subtypes expressing known immunosuppressive genes, grouped and colored by NET site.

motivated us to investigate the exhaustion phenotypes present in infiltrating CD8⁺ T cells. For this analysis, we included all cell types with nonzero expression of *CD8A* or *CD8B*: 4-1BB-hi CD8⁺ T cells, 4-1BB-lo CD8⁺ T cells, and MAITs. We first isolated all CD8⁺ cells from our T and NK cell dataset, which yielded two major subclusters (Fig. 3C). One cluster contained mostly 4-1BB-hi CD8⁺ T cells from the gNET sample, while the other cluster represented a mixture of all three CD8⁺ T cell types from all GEP-NET sites of origin. To further delineate CD8⁺ T cell subtypes, we interrogated the transcription expression patterns of genes previously identified in stem-like T cells (*TCF7*), memory T cells (*IL7R* and *CCR7*), activated T cells (*CD27*), and exhausted T cells (*TOX* and *HAVCR2/TIM3*) (Fig. 3D). Expression levels of *TCF7* and *IL7R* were highest in MAIT and 4-1BB-lo CD8⁺ T cells, while *TOX* and *TIM3* displayed the exact opposite expression pattern. These findings are consistent with previous single-cell analyses in renal cell carcinoma, which identified high expression of exhaustion markers among 4-1BB-hi CD8⁺ T cells (30).

To evaluate the potential therapeutic targets in the GEP-NET milieu using current immunotherapies, we quantified the expression of known, lymphoid-intrinsic immune checkpoint ligands on the T and NK cells in our atlas. *CTLA4* and *TIGIT* were expressed robustly and frequently in T_{regs} across all GEP-NET subtypes (i.e., pNETs, siNETs, and gNETs) (Fig. 3E). *LAG3*, *HAVCR2* (encoding *TIM3*), and *PDCD1* (encoding PD-1) were sparsely expressed in T and NK cells from pNETs and siNETs. The lymphoid compartment of our one gNET sample demonstrated the highest expression of all queried immunosuppressive markers, with up-regulation in the 4-1BB-hi CD8⁺ T cell, T_{regs}, *FGFBP2*⁻ NK cell, and cycling populations (Fig. 3E). The gNET sample had the highest World Health Organization (WHO) Grade [grade 3 (G3)] of all analyzed samples and was the only tumor to receive treatment with everolimus and chemotherapy in addition to a somatostatin analog (Fig. 1B), which may influence the up-regulation of immune checkpoint expression in its T and NK cells. Determining the roles of grade and treatment history in this phenomenon will necessitate expanded serial biopsy cohorts for future analysis.

Myeloid cells in GEP-NETs express targetable immunosuppressive ligands

Given the limited expression of classical immune checkpoint ligands and receptors on lymphoid cells in the GEP-NET microenvironment, we next sought to characterize the myeloid cells within our cohort. We subset all myeloid cells ($n = 4820$ cells) from our original dataset using known marker genes and reclustered them to identify monocytes (*CD16*⁺ and *CD16*⁻), DCs (*CLEC10A*-high DCs, *CLEC9A*-high DCs, and *CD207*⁺ DCs), and tumor-associated macrophages (*FOLR2*-high TAMs and *SELENOP*-high TAMs) (Fig. 4A and fig. S4, A and B). The proportion of myeloid cell types was similar across all tumors, and we did not identify any patient-specific or GEP-NET subtype-specific myeloid populations (Fig. 4A).

To determine whether myeloid cells in GEP-NETs expressed targetable immune checkpoint ligands, we then quantified the expression of immunosuppressive genes across our nine myeloid clusters. As in the tumor compartment, *PDL1* and *PDL2* were expressed in fewer than 20% of any given myeloid subtype (Fig. 4B). *VSIG4*, an inhibitor of both cytotoxic T cell and proinflammatory macrophage activation, was expressed most strongly in *FOLR2*-hi TAMs (31, 32).

Both *TIM3* and its binding partner Galectin-9 were more broadly expressed across both TAM and DC subtypes, suggesting an ability of these cells to suppress the activity of cytotoxic T cells. Last, the immunosuppressive ligands *VSIR* and *SIGLEC10*, which regulate antitumoral macrophage activity, displayed robust expression across the myeloid compartment; *VSIR* specifically was expressed in over 60% CD16⁺ monocytes and in more than half of *SELENOP*-hi and *FOLR2*-hi TAMs (33).

To better define the diversity of tumor-infiltrating macrophage phenotypes in GEP-NETs, we isolated the four TAM clusters and performed single-cell pathway enrichment analysis using the HALLMARK genesets from the Molecular Signature Database (Methods). The most significantly enriched pathways included (i) tumor necrosis factor- α (TNF- α) signaling via nuclear factor κ B, (ii) interferon- γ (IFN- γ) response, (iii) interleukin-2 (IL-2)/signal transducers and activators of transcription 5 (STAT5) signaling, and (iv) genes involved tumor growth factor- β signaling. Using the signature scoring protocol outlined in Neftel *et al.* (34), we then scored each TAM for expression of each of the four geneset signatures, also referred to as metamodules. We visualized the results of this scoring analysis as a two-dimensional butterfly plot wherein each quadrant represents a specific metamodule (Fig. 4C, left). *FOLR2*-hi TAMs scored highly across all four metamodules, while *SELENOP*-hi TAMs predominantly expressed TNF- α signaling and IFN- γ response genes (Fig. 4C, center). Grouping TAMs by tumor site of origin revealed that while TAMs from pNETs span all four metamodules, TAMs from siNETs and the gNET predominantly differentially score for the IFN- γ response signature (Fig. 4C, right).

Next, we assessed whether GEP-NET TAMs could be defined according to the traditional, albeit debated, M1 versus M2 macrophage binary classification system (35, 36). M1 macrophages are generally considered proinflammatory and antitumoral, whereas M2 macrophages display immunosuppressive activity. To this end, we scored all TAMs in our cohort for curated gene signatures for M1 or M2 macrophage states (Fig. 4D). Consistent with similar single-cell analyses in other cancer types, GEP-NET TAMs did not separate neatly into M1 or M2 groupings; for example, *FOLR2*-hi TAMs scored relatively highly for both the M1 and M2 signatures.

We next sought to determine whether GEP-NET infiltrating TAMs displayed different chemokine profiles depending on the tumor site of origin. We performed a differential gene expression analysis within all TAMs in a given subtype grouped by tumor site of origin (i.e., pancreatic, small intestinal, or gastric) and examined the top five differentially expressed genes (Fig. 4E). All TAMs originating from pNETs displayed increased expression of chemokines *CCL3*, *CCL4*, *CCL4L2*, and *CCL3L1* (Fig. 4, E and F). *FOLR2*-hi TAMs from siNETs differentially expressed chemokine *CCL24*, while *FOLR2*-hi TAMs and *SELENOP*-hi TAMs in the gNET sample had the highest expression of *CXCL9* and *CXCL10* (Fig. 4, E and F). *CCL3*, *CCL4*, *CXCL9*, and *CXCL10* are known to recruit activated T cells via binding to the *CXCR3* receptor, suggesting that *FOLR2*-hi and *SELENOP*-hi TAM subtypes identified in our cohort may have a role in orchestrating the antitumoral immune response in pNETs and gNETs. *CCL24* has been implicated in activation of the M2 macrophage phenotype; *SELENOP*-hi TAMs in our siNETs may therefore contribute to a protumoral microenvironment. In summary, our results demonstrate the heterogeneity within the

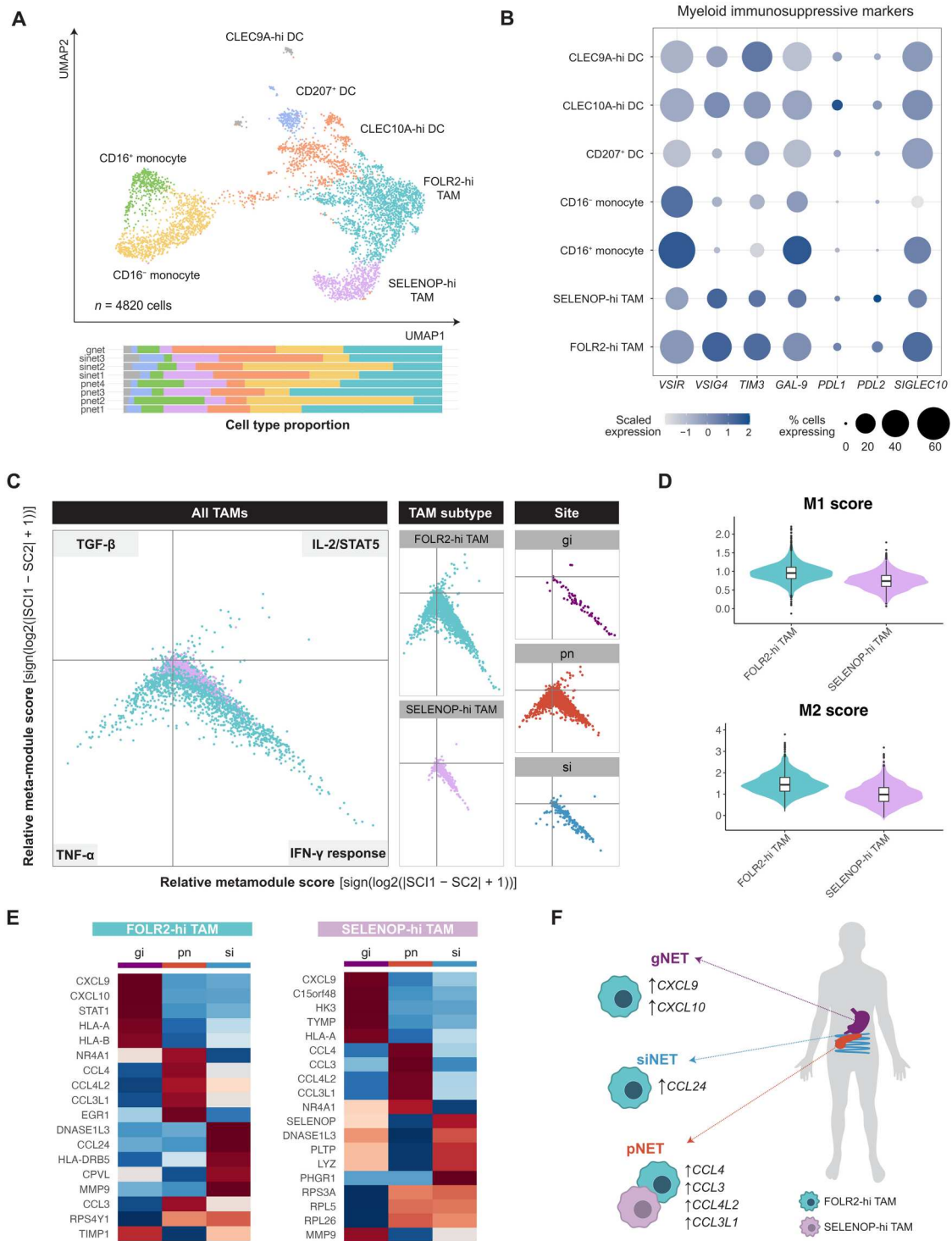


Fig. 4. GEP-NET–intrinsic myeloid cells express targetable immunosuppressive ligands. (A) UMAP of myeloid cells (top) from all tumors, colored and labeled by myeloid cell subtype. Barplot (bottom) displays myeloid cell type proportion by sample. (B) Dotplot of percentage of each myeloid subtype expressing immunosuppressive ligand genes. (C) Two-dimensional butterfly plot visualizations of relative metamodule scores of top MSigDB Hallmark Pathways (TNF- α , “TNFA Signaling Via NFKB;” IFN- γ , “Interferon Gamma Response;” IL-2/STAT5, “IL2 STAT5 Signaling;” and complement = “Complement”) in all GEP-NET–associated macrophages (left) and separated by TAM subtype (right). (D) Violin plot of VISION scores of M1 macrophage– and M2 macrophage–associated gene signatures, grouped by TAM subtype. (E) Heatmaps of scaled, normalized, and averaged expression of top differentially expressed genes between GEP-NET sites within each TAM subtype (left, FOLR2-hi TAMs and right, SELENOP-hi TAMs). (F) Graphical summary of differential chemokine expression patterns between TAMs from GEP-NETs at different anatomical sites.

myeloid compartments of GEP-NETs and highlight promising therapeutic vulnerabilities common across GEP-NET subtypes.

Charting the transcriptional heterogeneity and evolution dynamics between a primary siNET and its metastasis

Our cohort contained a matched primary-metastasis pair from a patient with siNET, which provided a rare opportunity to investigate the temporal evolution of GEP-NETs. We separated cells from the primary tumor (sinet2) and its liver metastasis (sinet3) for combined analysis (Fig. 5A). Both tumors contained a similar diversity of immune cells despite their different anatomical locations (Fig. 5A). We then sought to compare the transcriptomic landscapes of the paired samples. Selection and unsupervised

reclustering of only malignant cells from both tumors revealed four tumor clusters (Fig. 5B). Sinet2, the primary tumor, comprised mostly cells from cluster 0 (C0), with a minority of cells distributed throughout the other three clusters (Fig. 5C). Conversely, malignant cells from sinet3 fell predominantly in C1 and C2; no cells from the metastasis were found in C0 (Fig. 5C).

To interrogate the differences in transcriptional programming between each tumor cluster, we next conducted differential gene expression analysis on the malignant cells from sinet2 and sinet3 (Methods). We identified high expression of immediate early genes such as *JUN*, *FOS*, and *EGR1* in C0; expression of these genes was also identified in tumor C3 (Fig. 5D). C1 and C2 were distinguished from the other two clusters by differential expression

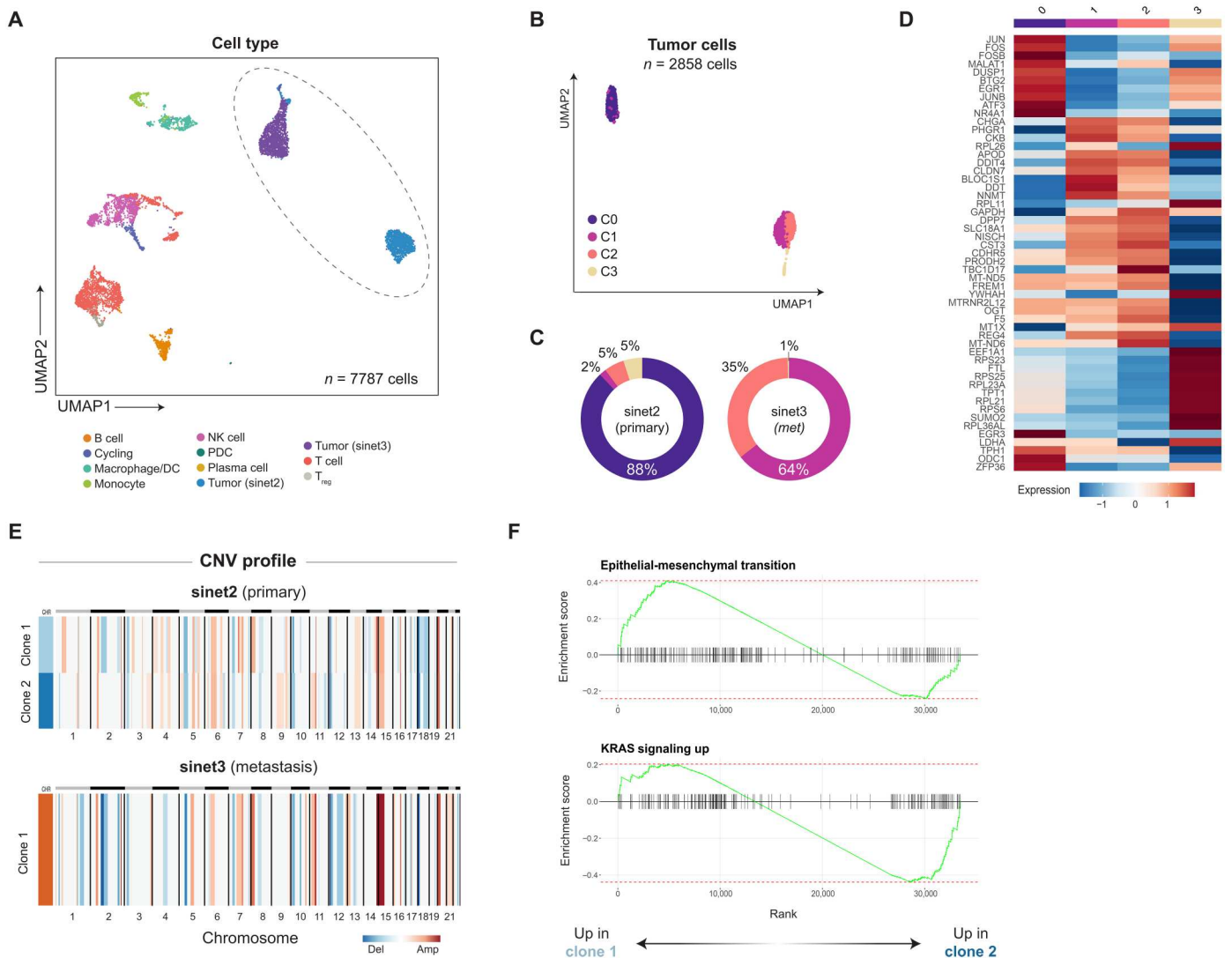


Fig. 5. scRNA-seq reveals intratumoral heterogeneity and evolution dynamics in GEP-NETs. (A) UMAP of malignant and immune cells from a primary siNET (sinet2) and its paired liver metastasis from the same patient (sinet3). Cells are colored by cancer or immune cell type. Tumor cells are represented by the clusters within the dashed oval. (B) UMAP of only tumor cells from sinet2 and sinet3, colored by Louvain cluster. (C) Donut plots representing percentage of cells found in each cluster from (B) for sinet2 and sinet3. Plots are colored by clusters as in (B). (D) Heatmap of scaled, normalized, and averaged expression of the top 10 differentially expressed genes between tumor clusters from (B). (E) Copy number alteration profiles of sinet2 and sinet3. Tumor subclones are indicated by color bars on the left-hand side of each plot. (F) GSEA of epithelial-mesenchymal transition (top) and KRAS signaling up (bottom) transcriptional signatures in clone 1 cells compared to clone 2 cells from sample sinet2.

of neuroendocrine genes such as *CHGA* and *SLC18A1*. Given that C1 and C2 contained mostly cells from sinet3, these data reflect the course of metastatic evolution of sinet2.

To better understand the differential genetic alterations between the primary tumor and its metastasis, we inferred copy number variation profiles for both tumors. The primary tumor (sinet2) contained two clones, with clone 1 distinguished from clone 2 by amplifications in chromosomes 1 and 8 and deletions in chromosome 2 (Fig. 5E). Next, we sought to interrogate differences in genetic programming between the subclones within sinet2 using gene set enrichment analysis (GSEA; Methods). Clone 1 demonstrated a high enrichment score for the HALLMARK "Epithelial-Mesenchymal Transition" geneset, implicating this subclone as a potential cellular origin for the liver metastasis (Fig. 5F). Clone 2 was enriched for the HALLMARK "KRAS Signaling Up" geneset (Fig. 5F). While KRAS mutations have been identified in high-grade pancreatic neuroendocrine carcinomas, further research is required to understand the potential role of KRAS signaling in GEP-NET oncogenesis and progression (37). Together, our findings further support the observation of metastatic transcriptional reprogramming in NETs.

DISCUSSION

To elucidate the fundamental cellular compositions and genetic programming of GEP-NETs, we interrogated single-cell transcriptomes from eight tumors spanning three anatomical sites of origin. Within our findings are reflections of known biology of NETs. For example, pNETs uniformly demonstrated high differential expression of endocrine pancreatic genes and displayed more intertumoral heterogeneity compared to other NET subtypes. siNETs expressed genes associated with monoamine synthesis and neuroendocrine vesicle biology, consistent with the known tendency of these tumors to secrete serotonin. Through scRNA-seq analysis, however, we were also able to further elucidate the transcriptional and GRN heterogeneity of GEP-NETs. Across our GEP-NET samples, we identified differentially expressed regulons with established roles in neuroendocrine cell differentiation and fate determination that expressed across various time points of gastrointestinal development. We further found that the transcriptional profiles of malignant pNET cells resemble more than one cell type in the mature human pancreatic islet, including somatostatin-producing delta cells and pancreatic polypeptide-producing gamma cells. These data imply the potential for lineage plasticity in GEP-NETs or an endocrine precursor cell provenance for these tumors, two possibilities that should be explored in future biological investigations.

The evolution of NETs as they metastasize remains poorly understood. While our sample size was limited, we were able to identify two subclones within one of our primary siNETs, one of which bore transcriptomic and copy number alteration similarities to the tumor cells in the patient's liver metastasis. Cells with robust expression of the neuroendocrine genes *CHGA* and *SLC18A1* comprised less than 15% of tumor cells at the primary tumor site but 100% of cells in the metastasis, suggesting that a phenotypic shift occurred over the course of tumor progression and metastasis. Our study is the first to demonstrate the transcriptional dynamics of metastatic NETs at single-cell resolution; future studies are warranted to

investigate the functional and translational significance of the transcriptional programs we identified in our work.

Immunotherapy has revolutionized cancer treatment over the past few decades and has demonstrated benefit across several solid tumor types. Recent clinical trials investigating immunotherapy in neuroendocrine cancers have focused on targeting classical checkpoint genes such as *CTLA4* and the *PD1-PDL1/PDL2* axes in the lymphoid compartment (38, 39). While many of these studies are ongoing, preliminary results suggest that undifferentiated, higher-grade neuroendocrine neoplasms may respond to checkpoint inhibition, but that use of checkpoint inhibitors in well-differentiated NETs, like those in our study, would yield limited therapeutic benefit (40–43). Consistent with these clinical observations, within all GEP-NET cancer cells in our dataset, we identified little to no expression of currently targetable immune checkpoint ligands, highlighting the limited treatment options in this disease. Similarly, within the lymphoid compartment of GEP-NETs, we further identified relatively low expression of common immunosuppressive ligands and receptors across T and NK cell types. 4-1BB-hi CD8⁺ T cells and *FGFBP2*[−] NK cells from our gNET exhibited the highest expression of immune checkpoint genes; however, this sample was the only higher grade (WHO G3) tumor of our cohort and the only one to receive somatostatin analog therapy, everolimus, and chemotherapy, all factors that could have contributed to this finding. Further translational studies will be required to determine the clinical utility of targeting lymphoid cells with immunotherapy in well-differentiated NETs.

In contrast, within the myeloid compartment, we observed high levels of immunosuppressive gene expression in multiple cell types across GEP-NET sites of origin and within both primary and metastatic tumors (fig. S5). Our data highlight opportunities for therapeutic strategies in these rare cancers based on targeting alternative pathways in the myeloid microenvironment of GEP-NETs. For instance, high expression of *VSIR* across myeloid cells in GEP-NETs suggests that targeting the VISTA protein could rearm T cells and macrophages and thereby reinvigorate antitumoral immunity in these patients. Preclinical studies of the VISTA pathway in multiple solid tumor models (e.g., pancreatic cancer, melanoma, colorectal cancer, renal cell carcinoma, and glioma) have affirmed its role in tumoral immune evasion (33, 44, 45). Early clinical trial data are assessing the safety profiles of anti-VISTA immunotherapies in solid tumors that also target the PD-1/PD-L1 checkpoint; per our findings, well-differentiated NETs may benefit from this therapeutic approach and should be considered for inclusion in future trial cohorts (46, 47). Similarly, we identified expression of *HAVCR2* (TIM3) and *LGALS9* (Gal-9) in myeloid cells of the GEP-NET microenvironment. Combination anti-Tim3/anti-PD-1 or anti-Gal-9/anti-PD-1 therapies have proven efficacious in enhancing T cell activation in preclinical studies of solid tumors and are currently under investigation in clinical trials (48–50). Last, inhibitors of SIGLEC10-CD24 binding between TAMs and cancer cells, respectively, are an emerging focus of preclinical investigation (51). Our study therefore provides evidence supporting the use of these emerging immunotherapies, which may one day augment the limited effective treatment options available to patients with nonresectable GEP-NETs.

Our study has several limitations. While the diversity of our cohort permits us to assess shared transcriptional programs across GEP-NET subtypes, our sample size remains relatively small due to

the rarity of these tumors. Treatment history at the time of surgical resection also varied between cases; all pNETs and one of the siNETs were treatment naïve, while the metastatic small intestinal and gNETs had received at least somatostatin analog therapy. Differences in cellular phenotypes and microenvironment composition may therefore reflect therapeutic pressures and not necessarily innate biology. To assess these possibilities, future studies should interrogate large, clinically diverse tumor cohorts that include GEP-NET subtypes and treatment modalities not represented in our study. Inclusion of more treatment-naïve cases can also help to better define innate tumor biology. Last, we here present an analysis of a singular well-differentiated, G3 gNET, a classification defined by the highest mitotic index out of all well-differentiated NETs. Given the high degree of similarity between well-differentiated G3 GEP-NETs and poorly differentiated, aggressive neuroendocrine carcinomas, identification, and inclusion of G3 GEP-NETs in studies of well-differentiated tumors demands careful review by experienced pathology teams. Despite the heterogeneity of cases included in our study, our cohort encompasses multiple, well-differentiated GEP-NET subtypes across diverse treatment histories; our findings therefore serve as a key foundation for future basic and clinical investigations into these rare, heterogeneous tumors. We anticipate that in addition to further evaluating our finding of common immunosuppressive myeloid phenotypes, new axes of shared biology can be identified through future multimodal sequencing of the transcriptional and epigenomic landscapes of GEP-NETs.

From a technical perspective, although we were able to infer copy number alteration profiles for each tumor using the inferCNV approach, verification of these inferred profiles will require patient-matched whole-genome sequencing. Overall, inferring tumor subclone architecture from single-cell data remains a challenging problem for the field given the sparsity and sampling biases inherent to scRNA-seq. Future work that obtains matched scRNA-seq and whole-genome sequencing can robustly characterize malignant subclones and also examine the influence of a GEP-NET patient's genetic background on their tumor's cellular landscape.

In summary, our findings uncover previously unappreciated heterogeneity within NET subtypes and reveal potential evolution in tumor characteristics as they metastasize. Consistent with other studies, we also found that in well-differentiated NETs, expression of checkpoint markers targetable with current standard immunotherapies is uncommon. However, we also identified immunosuppressive markers in myeloid cells that are commonly expressed in NETs and may form the basis for future targeted therapies. Our findings therefore provide an important step in delineating key underlying molecular features of NETs and shed light on potential novel therapeutic strategies for patients suffering from this challenging disease.

METHODS

Experimental model and subject details

Human patient samples were collected under Dana-Farber Cancer Institute IRB protocol #02-314. Informed consent was required for this study and was obtained as follows: At the time of their clinic appointments, patients were contacted by a member of the study staff and asked if they were interested in participating in this research study involving collection of biological samples and clinical

data in patients with NETs. The study was explained in detail to interested patients, and his/her questions were answered. Informed consent was signed to participate. Patients were specifically consented to (i) allow the collection of tissue, blood, or urine; (ii) to allow the collection and linkage of clinical data to the tissue; (iii) to allow for recontact of the patient for the purpose of recruitment into new clinical protocols, or for the purpose of obtaining clinical follow-up; (iv) to allow for a one-time additional blood draw or urine collection for study purposes if not feasible in the context of a scheduled blood draw; and (v) collection of periodic blood samples. The consent status of each patient was recorded in the database, which allows specific tailoring of data acquisition according to each patient's wishes. These measures will ensure that the wishes of each patient are maintained.

Methods details

Sample collection and dissociation for scRNA-seq

Fresh tissue from surgical resections was collected at Brigham and Women's Hospital. Members of the pathology team evaluated surgical specimens to identify tumor tissue. Tumor tissue that was not required for routine clinical pathological assessment was dissected away from nontumor tissue using a scalpel and transferred to a 50-ml conical tube with Hank's balanced salt solution and transported on ice. On arrival to the laboratory, tumor samples were transferred into a 5-ml Eppendorf tube containing 4.5-ml cold enzymatic dissociation mix [collagenase type 4 (100 µg/ml; Worthington Biochemical Corporation, #LS004186) and deoxyribonuclease I (100 µg/ml; StemCell Technologies, #07900) in RPMI + Hepes (Thermo Fisher Scientific, #22400089)]. The resection tissue was then minced inside the tube with spring scissors into <0.5-mm fragments at room temperature. The resulting mixture was incubated for 10 min in a 37°C water bath with manual inversions every 1 to 2 min to ensure thorough mixing. Next, the mixture was vigorously and repeatedly pipetted using a P1000 pipette at room temperature for further mechanical dissociation. For all samples except pnet2 and pnet3, the tube containing the mixture was then returned to the 37°C water bath for an additional 10 min with manual inversions every 1 to 2 min for thorough mixing.

The cell suspension was then filtered through a 70-µm cell strainer into a 15-ml conical tube on ice. The strainer was washed with 5-ml cold RPMI to maximize cellular yield. The filtered cells then underwent centrifugation at 450g for 5 min at 4°C. The resulting supernatant was carefully transferred to a 15-ml conical tube on ice, taking care not to disturb the pellet. To lyse red blood cells, the centrifuged cell pellet was resuspended in 300 to 500 µl of ACK lysing buffer (Thermo Fisher Scientific, #A1049201) and incubated for 1 min on ice. Calcium- and magnesium-free phosphate-buffered saline (PBS; Thermo Fisher Scientific, #10010-23) was added in a volume twice that of the ACK lysing buffer to stop red blood cell lysis. Cells were transferred to a 1.7-ml Eppendorf tube on ice and then recentrifuged for 8 s at 4°C with centrifugal force ramping up to but not exceeding 11,000g. After recentrifugation, cells were resuspended in calcium- and magnesium-free PBS with 0.4% bovine serum albumin (BSA; Ambion, #AM2616). If a large amount of red blood cells remained after recentrifugation, an additional round of red blood cell lysis was performed. After satisfactory red blood cell lysis, the supernatant was carefully transferred to a new 15-ml conical tube on ice, and the remaining cell pellet was resuspended in 50 µl of RPMI + Hepes.

Five microliters of the single-cell suspension was mixed with Trypan blue (Sigma-Aldrich, #T8154) at a 1:1 volume ratio and loaded into a hemocytometer for cell counting and assessment of cell viability, clumping, and debris. At the end of processing, all samples had viability greater than 51%. Cell suspensions were then centrifuged and resuspended in either RPMI + Hepes or RPMI + Hepes with 0.4% BSA in preparation for transport and downstream flow cytometric processing.

Flow cytometry

Following viability assessment, samples were centrifuged at 600g for 5 min and resuspended in fluorescence-activated cell sorting (FACS) buffer [1% BSA (Millipore Sigma, product no. EM-2930) in calcium/magnesium-free PBS (Thermo Fisher Scientific, product no. 14190144)] and stained with 1 μ g of CD45-APC antibody (Thermo Fisher Scientific, product no. 50-166-056) for 30 min at 4°C. The samples were washed with 1 ml of FACS buffer and centrifuged at 600g for 5 min before being resuspended in 100 μ l of FACS buffer with 10 μ M Stemolecule Y27632 (ROCK inhibitor) (Stemgent, product no. 04-0012-02). A total of 200 μ l of FACS buffer with calcein blue AM (Thermo Fisher Scientific, product no. C1429) was added to the sample for live/dead exclusion and the sample was passed through a 35- μ m strainer before sorting. Two fractions of the samples (live and CD45⁺) were sorted into FACS buffer using a Beckman Coulter MoFlo Astrios cytometer.

Single-cell RNA sequencing

For each sample, the live bulk and CD45⁺ fractions were centrifuged at 600g for 5 min and resuspended in FACS buffer for a final concentration of 600 cells/ μ l as specified in the 10x Genomics user guide document number CG000185, Rev. B for an estimated recovery of 3000 cells. These fractions were loaded into the 10x Genomics Single Cell chip (10x Genomics, #PN-1000120) along with gel beads and reverse transcription master mix from the Single Cell 5' v1.1 Chemistry Kit (10x Genomics, #PN-1000165). The chip was run on the 10x Chromium Controller using the standard program to produce complementary DNA, which was then amplified and used for Gene Expression (GEX) library generation. All single-cell GEX libraries were sequenced using an Illumina NextSeq 2000 sequencer.

scRNA-seq data preprocessing

Raw sequencing data underwent demultiplexing, barcode processing, read alignment, and UMI counting using the 10x Genomics Cell Ranger pipeline (version 5.0) with default parameters. Reads were aligned to the prebuilt human genome reference included in Cell Ranger (GRCh38). After filtering to exclude low-RNA content droplets, a gene-barcode matrix was generated for each sample containing counts of confidently mapped, non-PCR-duplicate reads.

To remove technical artifacts arising from cell-free RNA profiles from our sequencing data, ambient RNA decontamination was performed on all samples using the CellBender software package (52). In brief, the raw counts matrix and expected cell count for each sample were provided as input to the remove-background module of CellBender, which uses an unsupervised deep-generative model to distinguish empty droplets from cell-containing ones. Expected cell count was derived from the estimate generated by Cell Ranger. All samples were run using the "ambient" model and default settings of 150 training epochs and false-positive rate of 0.01. Transcripts assigned to empty cells were iteratively detected and removed from the raw counts matrix by remove-background, yielding a "background-subtracted" cleaned counts matrix as output.

To remove multiplet artifacts caused by droplet encapsulation of more than one cell, we then performed doublet detection and removal on the CellBender-cleaned counts matrix using the Scrublet package (Python, version 0.2.2) (53). An expected doublet rate of 0.06 and manually selected doublet score thresholds were used to separate singlets from neotypic doublets in the resulting bimodal score distribution graphs. Presumed doublets were removed to create an ambient RNA-free, singlet-only cleaned counts matrix for downstream analysis. All further quality control, dimensionality reduction, unsupervised clustering, and differential expression analyses were performed using the Seurat R package (version 4.0.6) (54).

Cell type clustering and across-sample integration

Before clustering, the 16 datasets (one unsorted and one CD45⁺ sorted per sample) were merged into a single Seurat object. Cells with fewer than 200 genes or greater than 25% counts representing mitochondrial genes were removed from each sample. Genes detected in fewer than three cells per sample were also removed. The raw counts data were then normalized and scaled using the default log-normalization approach from the R package Seurat (version 4.0.6) (54).

Linear dimensional reduction was performed on the integrated and normalized counts matrix by running principal components analysis (PCA) on the 5000 most highly variable genes in our dataset. The first 30 principal components were used to perform Louvain clustering with a resolution parameter of 0.4. Uniform Manifold Approximation and Projection (UMAP) was then performed using the same principal components to visualize preliminary cell clusters from the nonintegrated dataset in two-dimensional space.

To mitigate technical and biological variation between samples, the merged dataset was integrated using the R package Harmony (version 0.1.0), with patient of origin as the primary source of variation (55). Harmony uses the PCA embeddings for each cell to iteratively generate multisample clusters, penalizing clustering arrangements that contain clusters with one or few samples represented. The final integrated dataset included 24,048 cells from the eight-tumor cohort.

Cell type visualization, and identification

To determine cell types within each cluster, differential gene expression analysis was performed by comparing cells from each cluster to all other cells using a two-sided Wilcoxon rank-sum test with applied Bonferroni correction for multiple comparison testing. Top differential genes within each cluster were used to assign cells into broad tumor and immune categories. For subclassification of immune cell types, lymphoid and myeloid cells were subset from the integrated dataset and clustered and UMAP projected using 30 principal components. The same differential gene expression analysis was used to identify T cell and myeloid types at higher resolution. CD8⁺ T cells and TAMs were further reclustered and reprojected to conduct similar cellular dissection.

Identification of cancer cells

To identify malignant cells, we first integrated both non-CD45⁺-sorted and CD45⁺-sorted datasets from the same tumor to generate a combined expression matrix. Each sample underwent Louvain clustering and UMAP projection to identify *PTPRC*⁺ (CD45⁺) and *PTPRC*⁻ clusters. We then used inferCNV (R, Terra implementation) to estimate the CNV profile of each log-normalized sample using all *PTPRC*⁺ cells as the reference group and all *PTPRC*⁻ cells

as the observation group. NET-related marker gene expression and presence of inferred copy number alteration as determined by inferCNV were combined to identify “tumor” cells within our cohort.

Differential expression, GSEA, and signature scoring

To minimize the effect of patient-specific expression patterns on our differential gene expression analysis of GEP-NET cells across anatomical subtypes (Fig. 2C), we averaged the expression of genes from all tumors from the same primary site of origin (i.e., pancreas or small intestine) and compared the two transcriptional profiles. To compare the transcriptomic profiles of cells from a paired primary (sinet2) and metastatic (sinet3) tumor set, differential gene expression analysis was performed using a two-sided Wilcoxon rank-sum test with Bonferroni correction applied. The \log_2 (fold change) values for each gene were used as ranks for pre-ranked GSEA, which was performed using the fgsea R package (version 1.20.0) (56). GSEA was performed using all HALLMARK, Kyoto Encyclopedia of Genes and Genomes, and Gene Ontology Biological Process gene sets from version 6.2 of the MSigDb as input (57). Significance level was set at $P < 0.05$ and false discovery rate < 0.25 .

Single-cell signature scoring was performed using the VISION R package (version 3.0.0) (58). Progenitor exhaustion and terminal exhaustion signatures derived from Bi *et al.* (30) were used to score CD8⁺ T cells from all tumors (Fig. 3F). Known macrophage, monocyte, and DC markers were used to generate custom gene signatures, which were then used for VISION scoring of the NET myeloid compartment (Fig. 3B).

SCENIC analysis and regulon inference

To identify differentially active GRNs in tumor cells across GEP-NETs, we performed SCENIC analysis using the recommended pipeline provided with the pySCENIC implementation (https://github.com/aertslab/SCENICprotocol/blob/master/notebooks/PBMC10k_downstream-analysis.html) (59, 60). We first performed GRN inference using the multiprocessing implementation of Arboreto to run GRNBoost2 on the count matrix containing averaged expression of tumor cells from each sample. We then ran the SCENIC implementation of cisTarget to predict regulons from the TF adjacencies matrix produced by GRNBoost2. Last, we used AUCell to generate regulon specificity scores for each tumor. As recommended in the pySCENIC documentation, we selected the top five regulons in each tumor ranked by AUC, then plotted the scaled scores for these regulons by tumor.

Metamodule scoring

To generate metamodule scores for TAMs in Fig. 4, we first used Seurat’s FindAllMarkers function to identify TAM cluster-specific marker genes. We then used the average \log_2 (fold change) of genes in our differential expression analysis as a ranking metric for GSEA analysis on all TAMs using the HALLMARK genesets from the MSigDB. Four of the most enriched pathways from this analysis were selected as biologically relevant metamodules. To score each TAM for expression of these four metamodules, we implemented the method developed in Neftel *et al.* (34) using the scrabble R package. In brief, a signature score (SC) is calculated for each cell by averaging the relative expression of the signature genes in that cell, then subtracting the average relative expression of a control geneset in the same cell. The control geneset is defined as previously (34). All cells were scored for each of the four metamodules. The position of each cell in the butterfly plot (Fig. 4C) was determined

by calculating $[\text{sign}(\text{SC1} - \text{SC2}) * \log_2(|\text{SC1} - \text{SC2}| + 1)]$ for both x and y coordinates.

Determination of CNV clonal structure

To determine the clonal variation between the primary (sinet2) and metastatic tumor cells (sinet3) from the same patient with a siNET, cells from both samples were processed using the pipelineCNA function from the R package SCEVAN (61). The “subclones” parameter was set to “TRUE” to enable analysis of clonal structure within each tumor. Heatmaps displaying inferred copy number loss/gain across chromosomes 1 to 22 and showcasing the number of inferred subclones were generated for each sample through the SCEVAN pipeline. To identify pathways enriched in clone 1 and clone 2 from the primary tumor (sinet2), differential gene expression was performed comparing the pseudobulked malignant cells from each clone using Seurat’s FindAllMarkers function. The resulting differential gene list for each clone was ranked by \log_2 fold change and used as input for GSEA using the fgsea package (R, version 3.17).

Multiplex immunofluorescence staining and imaging

Multiplex immunofluorescence staining was performed on five FFPE samples from our cohort using a BOND RX fully automated stainer (Leica Biosystems). FFPE tissue sections of 5 μm thick are baked for 3 hours at 60°C before loading into the BOND RX. Slides are deparaffinized (BOND DeWax Solution, Leica Biosystems, catalog no. AR9590) and rehydrated with series of graded ethanol to deionized water. Antigen retrieval is performed in BOND epitope retrieval solution 1 (pH 6) or 2 (pH 9), as shown in table S2 (ER1 and ER2, Leica Biosystems, catalog nos. AR9961 and AR9640) at 95°C. Deparaffinization, rehydration, and antigen retrieval are preprogrammed and executed by the BOND RX. Slides are then serially stained with primary antibodies. Incubation time per primary antibody was 30 min. Subsequently, anti-mouse plus anti-rabbit Opal Polymer Horseradish Peroxidase (Opal Polymer HRP Ms. + Rb, Akoya Biosciences, catalog no. ARH1001EA) is applied as a secondary label with an incubation time of 10 min. Signal for antibody complexes is labeled and visualized by their corresponding Opal Fluorophore Reagents (Akoya Biosciences) by incubating the slides for 10 min. Opal Fluorophore 780 is paired with a TSA-DIG amplification to ensure adequate and analyzable signal. Slides are incubated in Spectral DAPI solution (Akoya Biosciences) for 10 min, air dried, and mounted with Prolong Diamond Antifade mounting medium (Life Technologies, catalog no. P36965) and stored in a light-proof box at 4°C before imaging. The target antigens, antibody clones, dilutions for markers, diluents, and antigen retrieval details are listed in table S2.

Image acquisition is performed using the PhenoImager multispectral imaging platform (Akoya Biosciences, Marlborough, MA). Each slide is scanned at 20 \times resolution as whole-slide scan images. These images are then accessible through Phenochart viewing software (Akoya Biosciences) where four to eight 20 \times regions of interest (ROIs) are selected. On the basis of well-staining tissue availability, three to seven ROIs per sample were chosen for analysis by a board-certified anatomic and molecular pathologist specialized in tissue-based biomarker assays. ROIs were chosen based on high tumor content; areas of necrosis, fibrosis, and unusual vascular architecture were explicitly avoided.

After ROI selection and approval from a pathologist (S.R.), the images are spectrally unmixed and analyzed within Inform 2.6 (Akoya Biosciences). The ROIs are subsequently segmented and

quantified for expression of each marker using the Inform analysis tools. Data tables are exported from Inform and run through a custom data extraction pipeline to obtain cell population densities (number of cells per square millimeter) for each marker and/or combinations of markers.

Supplementary Materials

This PDF file includes:

Figs. S1 to S5

Tables S1 and S2

REFERENCES AND NOTES

- Z. Xu, L. Wang, S. Dai, M. Chen, F. Li, J. Sun, F. Luo, Epidemiologic trends of and factors associated with overall survival for patients with gastroenteropancreatic neuroendocrine tumors in the United States. *JAMA Netw. Open* **4**, e2124750 (2021).
- A. Dasari, C. Shen, D. Halperin, B. Zhao, S. Zhou, Y. Xu, T. Shih, J. C. Yao, Trends in the incidence, prevalence, and survival outcomes in patients with neuroendocrine tumors in the United States. *JAMA Oncol.* **3**, 1335–1342 (2017).
- M. Pavel, K. Öberg, M. Falconi, E. P. Krenning, A. Sundin, A. Perren, A. Berruti; SMO Guidelines Committee. Electronic address: clinicalguidelines@esmo.org, Gastroenteropancreatic neuroendocrine neoplasms: ESMO Clinical Practice Guidelines for diagnosis, treatment and follow-up. *Ann. Oncol.* **31**, 844–860 (2020).
- J. Hallet, C. H. L. Law, M. Cukier, R. Saskin, N. Liu, S. Singh, Exploring the rising incidence of neuroendocrine tumors: A population-based analysis of epidemiology, metastatic presentation, and outcomes. *Cancer* **121**, 589–597 (2015).
- M. Cives, J. R. Strosberg, Gastroenteropancreatic neuroendocrine tumors. *CA Cancer J. Clin.* **68**, 471–487 (2018).
- A. Scarpa, The landscape of molecular alterations in pancreatic and small intestinal neuroendocrine tumours. *Ann. Endocrinol.* **80**, 153–158 (2019).
- A. Scarpa, D. K. Chang, K. Nones, V. Corbo, A.-M. Patch, P. Bailey, R. T. Lawlor, A. L. Johns, D. K. Miller, A. Mafficini, B. Rusev, M. Scardoni, D. Antonello, S. Barbi, K. O. Sikora, S. Cingarlini, C. Vicentini, S. McKay, M. C. J. Quinn, T. J. C. Bruxner, A. N. Christ, I. Harliwong, S. Idrisoglu, S. McLean, C. Nourse, E. Nourbakhsh, P. J. Wilson, M. J. Anderson, J. L. Fink, F. Newell, N. Waddell, O. Holmes, S. H. Kazakoff, C. Leonard, S. Wood, Q. Xu, S. H. Nagaraj, E. Amato, I. Dalai, S. Bersani, I. Cataldo, A. P. D. Tos, P. Capelli, M. V. Davi, L. Landoni, A. Malpaga, M. Miotto, V. L. J. Whitehall, B. A. Leggett, J. L. Harris, J. Harris, M. D. Jones, J. Humphris, L. A. Chantrill, V. Chin, A. M. Nagrial, M. Pajic, C. J. Scarlett, A. Pinho, I. Rooman, C. Toon, J. Wu, M. Pinese, M. Cowley, A. Barbour, A. Mawson, E. S. Humphrey, E. K. Colvin, A. Chou, J. A. Lovell, N. B. Jamieson, F. Duthie, M.-C. Gingras, W. E. Fisher, R. A. Dagg, L. M. S. Lau, M. Lee, H. A. Pickett, R. R. Reddel, J. S. Samra, J. G. Kench, N. D. Merrett, K. Epari, N. Q. Nguyen, N. Zeps, M. Falconi, M. Simbolo, G. Butturini, G. Van Buren, S. Partelli, M. Fassin; Australian Pancreatic Cancer Genome Initiative, K. K. Khanna, A. J. Gill, D. A. Wheeler, R. A. Gibbs, E. A. Musgrove, C. Bassi, G. Tortora, P. Pederzoli, J. V. Pearson, N. Waddell, A. V. Biankin, S. M. Grimmond, Whole-genome landscape of pancreatic neuroendocrine tumours. *Nature* **543**, 65–71 (2017).
- C. Luchini, R. C. Grant, A. Scarpa, S. Gallinger, Microsatellite instability/mismatch repair deficiency in pancreatic cancers: The same or different? *Gut* **70**, 1809–1811 (2021).
- J. Han, R. A. DePinho, A. Maitra, Single-cell RNA sequencing in pancreatic cancer. *Nat. Rev. Gastroenterol. Hepatol.* **18**, 451–452 (2021).
- X. Zhang, L. Peng, Y. Luo, S. Zhang, Y. Pu, Y. Chen, W. Guo, J. Yao, M. Shao, W. Fan, Q. Cui, Y. Xi, Y. Sun, X. Niu, X. Zhao, L. Chen, Y. Wang, Y. Liu, X. Yang, C. Wang, C. Zhong, W. Tan, J. Wang, C. Wu, D. Lin, Dissecting esophageal squamous-cell carcinoma ecosystem by single-cell transcriptomic analysis. *Nat. Commun.* **12**, 5291 (2021).
- K. Pelka, M. Hofree, J. H. Chen, S. Sarkizova, J. D. Pirl, V. Jorgji, A. Bejnood, D. Dionne, W. H. Ge, K. H. Xu, S. X. Chao, D. R. Zollinger, D. J. Lieber, J. W. Reeves, C. A. Fuhrman, M. L. Hoang, T. Delorey, L. T. Nguyen, J. Waldman, M. Klapholz, I. Wakiro, O. Cohen, J. Albers, C. S. Smillie, M. S. Cuoco, J. Wu, M.-J. Su, J. Yeung, B. Vijaykumar, A. M. Magnuson, N. Asinowski, T. Moll, M. N. Goder-Reiser, A. S. Applebaum, L. K. Brais, L. K. DelloStritto, S. L. Denning, S. T. Phillips, E. K. Hill, J. K. Meehan, D. T. Frederick, T. Sharova, A. Kanodia, E. Z. Todres, J. Jané-Valbuena, M. Biton, B. Izar, C. D. Lambden, T. E. Clancy, R. Bleday, N. Melnitchouk, J. Irani, H. Kunitake, D. L. Berger, A. Srivastava, J. L. Hornick, S. Ogino, A. Rotem, S. Vignea, B. E. Johnson, R. B. Corcoran, A. H. Sharpe, V. K. Kuchroo, K. Ng, M. Giannakis, L. T. Nieman, G. M. Boland, A. J. Aguirre, A. C. Anderson, O. Rozenblatt-Rosen, A. Regev, N. Hacohen, Spatially organized multicellular immune hubs in human colorectal cancer. *Cell* **184**, 4734–4752.e20 (2021).
- S. Raghavan, P. S. Winter, A. W. Navia, H. L. Williams, A. DenAdel, K. E. Lowder, J. Galvez-Reyes, R. L. Kalekar, N. Mulugeta, K. S. Kapner, M. S. Raghavan, A. A. Borah, N. Liu, S. A. Väyrynen, A. D. Costa, R. W. S. Ng, J. Wang, E. K. Hill, D. Y. Ragon, L. K. Brais, A. M. Jaeger, L. F. Spurr, Y. Y. Li, A. D. Cherniack, M. A. Booker, E. F. Cohen, M. Y. Tolstourov, I. Wakiro, A. Rotem, B. E. Johnson, J. M. McFarland, E. T. Sicsinska, T. E. Jacks, R. J. Sullivan, G. I. Shapiro, T. E. Clancy, K. Perez, D. A. Robinson, K. Ng, J. M. Cleary, L. Crawford, S. R. Manalis, J. A. Nowak, B. M. Wolpin, W. C. Hahn, A. J. Aguirre, A. K. Shalek, Microenvironment drives cell state, plasticity, and drug response in pancreatic cancer. *Cell* **184**, 6119–6137.e26 (2021).
- C. S. Chan, S. V. Laddha, P. W. Lewis, M. S. Koletsy, K. Robzyk, E. Da Silva, P. J. Torres, B. R. Untch, J. Li, P. Bose, T. A. Chan, D. S. Klimstra, C. D. Allis, L. H. Tang, ATRX, DAXX or MEN1 mutant pancreatic neuroendocrine tumors are a distinct alpha-cell signature subgroup. *Nat. Commun.* **9**, 4158 (2018).
- B. L. Taylor, F.-F. Liu, M. Sander, Nkx6.1 is essential for maintaining the functional state of pancreatic beta cells. *Cell Rep.* **4**, 1262–1275 (2013).
- A. Swisa, D. Avrahami, N. Eden, J. Zhang, E. Feleke, T. Dahan, Y. Cohen-Tayar, M. Stolovich-Rain, K. H. Kaestner, B. Glaser, R. Ashery-Padan, Y. Dor, PAX6 maintains β cell identity by repressing genes of alternative islet cell types. *J. Clin. Invest.* **127**, 230–243 (2017).
- J. M. Servitja, J. Ferrer, Transcriptional networks controlling pancreatic development and beta cell function. *Diabetologia* **47**, 597–613 (2004).
- S. Rieck, E. D. Bankaitis, C. V. E. Wright, Lineage determinants in early endocrine development. *Semin. Cell Dev. Biol.* **23**, 673–684 (2012).
- B. K. Gage, A. Asadi, R. K. Baker, T. D. Webber, R. Wang, M. Itoh, M. Hayashi, R. Miyata, T. Akashi, T. J. Kieffer, The role of ARX in human pancreatic endocrine specification. *PLoS ONE* **10**, e0144100 (2015).
- P. Cejas, Y. Drier, K. M. A. Dreijerink, L. A. A. Brosens, V. Deshpande, C. B. Epstein, E. B. Conemans, F. H. M. Morsink, M. K. Graham, G. D. Valk, M. R. Vriens, C. F. Castillo, C. R. Ferrone, T. Adar, M. Bowden, H. J. Whitton, A. Da Silva, A. Font-Tello, H. W. Long, E. Gaskell, N. Shores, C. M. Heaphy, E. Sicsinska, M. H. Kulke, D. C. Chung, B. E. Bernstein, R. A. Shivdasani, Enhancer signatures stratify and predict outcomes of non-functional pancreatic neuroendocrine tumors. *Nat. Med.* **25**, 1260–1265 (2019).
- L. Wang, Y. Tang, H. Wu, G. Shan, TCF12 activates MAGT1 expression to regulate the malignant progression of pancreatic carcinoma cells. *Oncol. Lett.* **23**, 62 (2022).
- R. J. Pérez, Y. D. Benoit, L. J. Gudas, Deletion of retinoic acid receptor β (RAR β) impairs pancreatic endocrine differentiation. *Exp. Cell Res.* **319**, 2196–2204 (2013).
- M. O. Nandan, A. M. Ghaleb, A. B. Bialkowska, V. W. Yang, Krüppel-like factor 5 is essential for proliferation and survival of mouse intestinal epithelial stem cells. *Stem Cell Res.* **14**, 10–19 (2015).
- H. J. Li, S. K. Ray, N. Pan, J. Haigh, B. Fritzsche, A. B. Leiter, Intestinal NeuroD1 expression impairs paneth cell differentiation and promotes enteroendocrine lineage specification. *Sci. Rep.* **9**, 19489 (2019).
- D. Z. Ye, K. H. Kaestner, Foxa1 and Foxa2 control the differentiation of goblet and enteroendocrine L- and D-cells in mice. *Gastroenterology* **137**, 2052–2062 (2009).
- Y.-H. Hung, S. Huang, M. K. Dame, Q. Yu, Q. C. Yu, Y. A. Zeng, J. G. Camp, J. R. Spence, P. Sethupathy, Chromatin regulatory dynamics of early human small intestinal development using a directed differentiation model. *Nucleic Acids Res.* **49**, 726–744 (2021).
- L. van Gurp, L. Fodoulian, D. Oropeza, K. Furuyama, E. Bru-Tari, A. N. Vu, J. S. Kaddis, I. Rodríguez, F. Thorel, P. L. Herrera, Generation of human islet cell type-specific identity genesets. *Nat. Commun.* **13**, 2020 (2022).
- E. D. Carosella, N. Rouas-Freiss, D. T.-L. Roux, P. Moreau, J. LeMaout, “Chapter Two - HLA-G: An Immune Checkpoint Molecule” in *Advances in Immunology*, F. W. Alt, Ed. (Academic Press, 2015), vol. 127, pp. 33–144.
- C. D. Carey, D. Gusenleitner, M. Lipschitz, M. G. M. Roemer, E. C. Stack, E. Gjini, X. Hu, R. Redd, G. J. Freeman, D. Neuberg, F. S. Hodi, X. S. Liu, M. A. Shipp, S. J. Rodig, Topological analysis reveals a PD-L1-associated microenvironmental niche for Reed-Sternberg cells in Hodgkin lymphoma. *Blood* **130**, 2420–2430 (2017).
- J. C. Yao, M. H. Shah, T. Ito, C. L. Bohas, E. M. Wolin, E. Van Cutsem, T. J. Hobday, T. Okusaka, J. Capdevila, E. G. E. de Vries, P. Tomassetti, M. E. Pavel, S. Hoosen, T. Haas, J. Lincy, D. Lebwohl, K. Öberg; RAD001 in Advanced Neuroendocrine Tumors, Third Trial (RADIANT-3) Study Group, Everolimus for advanced pancreatic neuroendocrine tumors. *N. Engl. J. Med.* **364**, 514–523 (2011).
- K. Bi, M. X. He, Z. Bakouny, A. Kanodia, S. Napolitano, J. Wu, G. Grimaldi, D. A. Braun, M. S. Cuoco, A. Mayorga, L. DelloStritto, G. Bouchard, J. Steinharter, A. K. Tewari, N. I. Vokes, E. Shannon, M. Sun, J. Park, S. L. Chang, B. A. McGregor, R. Haq, T. Denize, S. Signoretti, J. L. Guerriero, S. Vignea, O. Rozenblatt-Rosen, A. Rotem, A. Regev, T. K. Choueiri, E. M. Van Allen, Tumor and immune reprogramming during immunotherapy in advanced renal cell carcinoma. *Cancer Cell* **39**, 649–661.e5 (2021).
- J. Li, B. Diao, S. Guo, X. Huang, C. Yang, Z. Feng, W. Yan, Q. Ning, L. Zheng, Y. Chen, Y. Wu, VSIG4 inhibits proinflammatory macrophage activation by reprogramming mitochondrial pyruvate metabolism. *Nat. Commun.* **8**, 1322 (2017).

32. L. Vogt, N. Schmitz, M. O. Kurrer, M. Bauer, H. I. Hinton, S. Behnke, D. Gatto, P. Sebbel, R. R. Beerli, I. Sonderegger, M. Kopf, P. Saudan, M. F. Bachmann, V5IG4, a B7 family-related protein, is a negative regulator of T cell activation. *J. Clin. Invest.* **116**, 2817–2826 (2006).
33. J. L. Lines, E. Pantazi, J. Mak, L. F. Sempere, L. Wang, S. O'Connell, S. Ceeraz, A. A. Suriawinata, S. Yan, M. S. Ernstoff, R. Noelle, VISTA is an immune checkpoint molecule for human T cells. *Cancer Res.* **74**, 1924–1932 (2014).
34. C. Neftel, J. Laffy, M. G. Filbin, T. Hara, M. E. Shore, G. J. Rahme, A. R. Richman, D. Silverbush, M. L. Shaw, C. M. Hebert, J. Dewitt, S. Gritsch, E. M. Perez, L. N. Gonzalez Castro, X. Lan, N. Druck, C. Rodman, D. Dionne, A. Kaplan, M. S. Bertalan, J. Small, K. Pelton, S. Becker, D. Bonal, Q.-D. Nguyen, R. L. Servis, J. M. Fung, R. Mylvaganam, L. Mayr, J. Gojo, C. Haberler, R. Geyeregger, T. Czech, I. Slavic, B. V. Nahed, W. T. Curry, B. S. Carter, H. Wakimoto, P. K. Brastianos, T. T. Batchelor, A. Stemmer-Rachamimov, M. Martinez-Lage, M. P. Frosch, I. Stamenkovic, N. Riggi, E. Rheinbay, M. Monje, O. Rozenblatt-Rosen, D. P. Cahill, A. P. Patel, T. Hunter, I. M. Verma, K. L. Ligon, D. N. Louis, A. Regev, B. E. Bernstein, I. Tirosh, M. L. Suvà, An integrative model of cellular states, plasticity, and genetics for glioblastoma. *Cell* **178**, 835–849.e21 (2019).
35. C. D. Mills, K. Kincaid, J. M. Alt, M. J. Heilman, A. M. Hill, M-1/M-2 macrophages and the Th1/Th2 paradigm. *J. Immunol.* **164**, 6166–6173 (2000).
36. A. Mantovani, A. Sica, S. Sozzani, P. Allavena, A. Vecchi, M. Locati, The chemokine system in diverse forms of macrophage activation and polarization. *Trends Immunol.* **25**, 677–686 (2004).
37. B. Konukiewitz, M. Jesinghaus, K. Steiger, A. M. Schlitter, A. Kasajima, B. Sipos, G. Zamboni, W. Weichert, N. Pfarr, G. Klöppel, Pancreatic neuroendocrine carcinomas reveal a closer relationship to ductal adenocarcinomas than to neuroendocrine tumors G3. *Hum. Pathol.* **77**, 70–79 (2018).
38. M. Albertelli, A. Dotto, F. Nista, A. Veresani, L. Patti, S. Gay, S. Sciallero, M. Boschetti, D. Ferone, Present and future of immunotherapy in neuroendocrine tumors. *Rev. Endocr. Metab. Disord.* **22**, 615–636 (2021).
39. T. Al-Toubah, M. Cives, J. Strosberg, Novel immunotherapy strategies for treatment of neuroendocrine neoplasms. *Transl. Gastroenterol. Hepatol.* **5**, 54 (2020).
40. J. M. Mehnert, E. Bergsland, B. H. O'Neil, A. Santoro, J. H. M. Schellens, R. B. Cohen, T. Doi, P. A. Ott, M. J. Pishvaian, I. Puzanov, K. L. Aung, C. Hsu, C. Le Tourneau, A. Hollebecque, E. Élez, K. Tamura, M. Gould, P. Yang, K. Stein, S. A. Piha-Paul, Pembrolizumab for the treatment of programmed death-ligand 1-positive advanced carcinoid or pancreatic neuroendocrine tumors: Results from the KEYNOTE-028 study. *Cancer* **126**, 3021–3030 (2020).
41. J. Strosberg, N. Mizuno, T. Doi, E. Grande, J.-P. Delord, R. Shapira-Frommer, E. Bergsland, M. Shah, M. Fakhri, S. Takahashi, S. A. Piha-Paul, B. O'Neil, S. Thomas, M. P. Lolkema, M. Chen, N. Ibrahim, K. Norwood, J. Hadoux, Efficacy and safety of pembrolizumab in previously treated advanced neuroendocrine tumors: Results from the phase II KEYNOTE-158 study. *Clin. Cancer Res.* **26**, 2124–2130 (2020).
42. O. Klein, D. Kee, B. Markman, M. Michael, C. Underhill, M. S. Carlino, L. Jackett, C. Lum, C. Scott, A. Nagrial, A. Behren, J. Y. So, J. Palmer, J. Cebon, Immunotherapy of ipilimumab and nivolumab in patients with advanced neuroendocrine tumors: A subgroup analysis of the CA209-538 clinical trial for rare cancers. *Clin. Cancer Res.* **26**, 4454–4459 (2020).
43. J. M. Mehnert, H. S. Rugo, B. H. O'Neil, A. Santoro, J. H. M. Schellens, R. B. Cohen, T. Doi, P. A. Ott, M. J. Pishvaian, I. Puzanov, Pembrolizumab for patients with PD-L1-positive advanced carcinoid or pancreatic neuroendocrine tumors: Results from the KEYNOTE-028 study. *Ann. Oncol.* **28**, v142 (2017).
44. X. Huang, X. Zhang, E. Li, G. Zhang, X. Wang, T. Tang, X. Bai, T. Liang, VISTA: An immune regulatory protein checking tumor and immune cells in cancer immunotherapy. *J. Hematol. Oncol.* **13**, 83 (2020).
45. J. Gao, J. F. Ward, C. A. Pettaway, L. Z. Shi, S. K. Subudhi, L. M. Vence, H. Zhao, J. Chen, H. Chen, E. Efstathiou, P. Troncoso, J. P. Allison, C. J. Logothetis, I. I. Wistuba, M. A. Sepulveda, J. Sun, J. Wargo, J. Blando, P. Sharma, VISTA is an inhibitory immune checkpoint that is increased after ipilimumab therapy in patients with prostate cancer. *Nat. Med.* **23**, 551–555 (2017).
46. J. Powderly, M. R. Patel, J. J. Lee, J. Brody, F. Meric-Bernstam, E. Hamilton, S. Ponce Aix, J. Garcia-Corbacho, Y.-J. Bang, M.-J. Ahn, S. Y. Rha, K.-P. Kim, M. Gil Martin, H. Wang, A. Lazorchak, T. Wyant, A. Ma, S. Agarwal, D. Tuck, A. Daud, CA-170, a first in class oral small molecule dual inhibitor of immune checkpoints PD-L1 and VISTA, demonstrates tumor growth inhibition in pre-clinical models and promotes T cell activation in phase 1 study. *Ann. Oncol.* **28**, v405–v406 (2017).
47. J. J. Lee, J. D. Powderly, M. R. Patel, J. Brody, E. P. Hamilton, J. R. Infante, G. S. Falchook, H. Wang, L. Adams, L. Gong, A. W. Ma, T. Wyant, A. Lazorchak, S. Agarwal, D. P. Tuck, A. Daud, Phase 1 trial of CA-170, a novel oral small molecule dual inhibitor of immune checkpoints PD-1 and VISTA, in patients (pts) with advanced solid tumor or lymphomas. *J. Clin. Oncol.* **35**, TPS3099 (2017).
48. K. Sakuishi, L. Apetoh, J. M. Sullivan, B. R. Blazar, V. K. Kuchroo, A. C. Anderson, Targeting Tim-3 and PD-1 pathways to reverse T cell exhaustion and restore anti-tumor immunity. *J. Exp. Med.* **207**, 2187–2194 (2010).
49. N. Acharya, C. Sabatos-Peyton, A. C. Anderson, Tim-3 finds its place in the cancer immunotherapy landscape. *J. Immunother. Cancer* **8**, e000911 (2020).
50. R. Yang, L. Sun, C.-F. Li, Y.-H. Wang, J. Yao, H. Li, M. Yan, W.-C. Chang, J.-M. Hsu, J.-H. Cha, J. L. Hsu, C.-W. Chou, X. Sun, Y. Deng, C.-K. Chou, D. Yu, M.-C. Hung, Galectin-9 interacts with PD-1 and TIM-3 to regulate T cell death and is a target for cancer immunotherapy. *Nat. Commun.* **12**, 832 (2021).
51. M. J. Pittet, O. Michielin, D. Migliorini, Clinical relevance of tumour-associated macrophages. *Nat. Rev. Clin. Oncol.* **19**, 402–421 (2022).
52. S. J. Fleming, J. C. Marioni, M. Babadi, CellBender remove-background: A deep generative model for unsupervised removal of background noise from scRNA-seq datasets. *bioRxiv* 2019.10.1101/791699 (2019). <https://doi.org/10.1101/791699>.
53. S. L. Wolock, R. Lopez, A. M. Klein, Scrublet: Computational identification of cell doublets in single-cell transcriptomic data. *Cell Syst.* **8**, 281–291.e9 (2019).
54. Y. Hao, S. Hao, E. Andersen-Nissen, W. M. Mauck, S. Zheng, A. Butler, M. J. Lee, A. J. Wilk, C. Darby, M. Zager, P. Hoffman, M. Stoeckius, E. Papalexi, E. P. Mimitou, J. Jain, A. Srivastava, T. Stuart, L. M. Fleming, B. Yeung, A. J. Rogers, J. M. McElrath, C. A. Blish, R. Gottardo, P. Smibert, R. Satija, Integrated analysis of multimodal single-cell data. *Cell* **184**, 3573–3587.e29 (2021).
55. I. Korsunsky, N. Millard, J. Fan, K. Slowikowski, F. Zhang, K. Wei, Y. Baglaenko, M. Brenner, P.-R. Loh, S. Raychaudhuri, Fast, sensitive and accurate integration of single-cell data with Harmony. *Nat. Methods* **16**, 1289–1296 (2019).
56. G. Korotkevich, V. Sukhov, N. Budin, B. Shpak, M. N. Artyomov, A. Sergushichev, Fast gene set enrichment analysis. *bioRxiv* 2021.10.1101/060012 (2021). <https://doi.org/10.1101/060012>.
57. A. Liberzon, C. Birger, H. Thorvaldsdóttir, M. Ghandi, J. P. Mesirov, P. Tamayo, The Molecular Signatures Database (MSigDB) hallmark gene set collection. *Cell Syst.* **1**, 417–425 (2015).
58. D. DeTomaso, M. G. Jones, M. Subramaniam, T. Ashuaach, C. J. Ye, N. Yosef, Functional interpretation of single cell similarity maps. *Nat. Commun.* **10**, 4376 (2019).
59. B. Van de Sande, C. Flerin, K. Davie, M. De Waegeneer, G. Hulselmans, S. Aibar, R. Seurinck, W. Saels, R. Cannoodt, Q. Rouchon, T. Verbeiren, D. De Maeyer, J. Reumers, Y. Saeys, S. Aerts, A scalable SCENIC workflow for single-cell gene regulatory network analysis. *Nat. Protoc.* **15**, 2247–2276 (2020).
60. S. Aibar, C. B. González-Blas, T. Moerman, V. A. Huynh-Thu, H. Imrichova, G. Hulselmans, F. Rambow, J.-C. Marine, P. Geurts, J. Aerts, J. van den Oord, Z. K. Atak, J. Wouters, S. Aerts, SCENIC: Single-cell regulatory network inference and clustering. *Nat. Methods* **14**, 1083–1086 (2017).
61. A. De Falco, F. Caruso, X.-D. Su, A. Iavarone, M. Ceccarelli, A fast variational algorithm to detect the clonal copy number substructure of tumors from single-cell data. *bioRxiv* 2021.11.20.469390 (2021). <https://doi.org/10.1101/2021.11.20.469390>.

Acknowledgments: We thank the patients who participated in this study. We are grateful to the Center for Immuno-Oncology at Dana-Farber Cancer Institute for assistance with the generation and interpretation of immunofluorescence images in patient samples. **Funding:** This work was supported by NIH grants T32 GM141745 (to S.E.H.), 5U2CCA233195-05 (to E.M.V.A.), R37 CA222574 (to J.P. and E.M.V.A.), and R01 CA227388 (to J.P. and E.M.V.A.); Bristol Myers Squibb (S.R.); KITE/Gilead (S.R.); the Goldhirsh-Yellin Foundation (M.H.K., J.Chan., and G.J.M.); and the Orr Family Foundation (S.E.H., J.Chan, and E.M.V.A.). The project described was supported by award numbers T32GM007753 (S.E.H.) and T32GM144273 (S.E.H.) from the National Institute of General Medical Sciences. The content is solely the responsibility of the authors and does not necessarily represent the official views of the National Institute of General Medical Sciences or the NIH. **Author contributions:** S.E.H.: conceptualization, formal analysis, writing—original draft, visualization, and methodology. T.W.D.: methodology, investigation, and writing—review and editing. C.V.M.: data curation and formal analysis. K.B.: writing—review and editing. B.T.: writing—review and editing. S.J.: writing—review and editing. L.D.: data curation and project administration. M.P.: investigation. C.M.: investigation. S.I.: investigation. J.Chen.: investigation. G.G.: investigation. S.N.: investigation. I.W.: investigation. J.Wu.: investigation. J.Y.: investigation. A.R.: investigation. Ew.S.: resources. Er.S.: project administration. T.C.: resources. J.Wa.: resources. S.D.: investigation. L.B.: project administration. N.R.B.: data curation, investigation, and formal analysis. K.L.P.: data curation and investigation. Y.H.: data curation and formal analysis. K.Z.K.: data curation and investigation. S.R.: supervision. J.L.H.: resources. S.V.: investigation and supervision. J.P.: writing—review and editing. M.H.K.: conceptualization, funding acquisition, supervision, and writing—review and editing. J.Chan.: conceptualization, funding acquisition, supervision, and writing—review and editing. E.M.V.A.: conceptualization, funding acquisition, supervision, writing—original draft, and writing—review and editing. G.J.M.: conceptualization, funding acquisition, supervision, and writing—review and editing.

Competing interests: A.R. is an equity holder in Celsius Therapeutics and NucleAI and reports a consulting relationship with eGenesis. J.C. reports consulting relationships with Advanced

Accelerator Applications and TerSera and equity in Merck. E.M.V.A. reports advisory and consulting relationships with Tango Therapeutics, Genome Medical, Genomic Life, Enara Bio, Janssen, Manifold Bio, and Monte Rosa; research support from Novartis and BMS; equity in Tango Therapeutics, Genome Medical, Genomic Life, Syapse, Enara Bio, Manifold Bio, Microsoft, and Monte Rosa; institutional patents filed on chromatin mutations and immunotherapy response and methods for clinical interpretation; intermittent legal consulting on patents for Foaley & Hoag; and serves on the Editorial Boards of JCO Precision Oncology and Science Advances. S.R. is a member of the SAB of Immunitas Therapeutics and receives research funding from KITE/Gilead and Bristol Myers Squibb. All other authors declare they have no competing interests. **Data and materials availability:** Raw scRNA-seq data will be deposited into dbGaP (accession number phs003141). Processed scRNA-seq data will be deposited into the Broad

Institute Single Cell Portal (https://singlecell.broadinstitute.org/single_cell). We will include annotations for all cells including patient of origin, tissue site, and cell type metadata used for this manuscript's analyses. All data needed to evaluate the conclusions in the paper are present in the paper and/or the Supplementary Materials. Code for analysis is described in the "Methods details" section above.

Submitted 15 July 2022

Accepted 24 August 2023

Published 27 September 2023

10.1126/sciadv.add9668

Intertumoral lineage diversity and immunosuppressive transcriptional programs in well-differentiated gastroenteropancreatic neuroendocrine tumors

Samantha E. Hoffman, Todd W. Dowrey, Carlos Villacorta Martin, Kevin Bi, Breanna Titchen, Shreya Johri, Laura DelloStritto, Miraj Patel, Colin Mackichan, Stephanie Inga, Judy Chen, Grace Grimaldi, Sara Napolitano, Isaac Wakiro, Jingyi Wu, Jason Yeung, Asaf Rotem, Ewa Sicinska, Erin Shannon, Thomas Clancy, Jiping Wang, Sarah Denning, Lauren Brais, Naomi R. Besson, Kathleen L. Pfaff, Ying Huang, Katrina Z. Kao, Scott Rodig, Jason L. Hornick, Sebastien Vigneau, Jihye Park, Matthew H. Kulke, Jennifer Chan, Eliezer M. Van Allen, and George J. Murphy

Sci. Adv. **9** (39), eadd9668. DOI: 10.1126/sciadv.add9668

View the article online

<https://www.science.org/doi/10.1126/sciadv.add9668>

Permissions

<https://www.science.org/help/reprints-and-permissions>

Use of this article is subject to the [Terms of service](#)

Science Advances (ISSN 2375-2548) is published by the American Association for the Advancement of Science. 1200 New York Avenue NW, Washington, DC 20005. The title *Science Advances* is a registered trademark of AAAS.

Copyright © 2023 The Authors, some rights reserved; exclusive licensee American Association for the Advancement of Science. No claim to original U.S. Government Works. Distributed under a Creative Commons Attribution NonCommercial License 4.0 (CC BY-NC).